Bulk and Nanocomposite Thermoelectrics: Synthesis, Properties, and Applications

Mustafa Shalaby, Salwa Hamdy, Ishtihadah Islam, Kulwinder Kaur, Aamer Nazir, and Shakeel Ahmad Khandy

Abstract Being a possible solution to avoid many environmental, political and economic issues, thermoelectric materials have been widely investigated for their ability to convert heat into electricity in the recent past as well as their benefit in reducing the dependence on fossil fuels. In this review we tried to highlight the challenges and possible strategies to synthesize efficient thermoelectric materials. The performance of thermoelectric power harvesting systems or thermoelectric generators (TEGs) relies on the improvement of the overall figure of merit (ZT) and the output power. Nanocomposite thermoelectrics display a vibrant augmentation of ZT and the strain engineering or band manipulation in bulk thermoelectrics prospect from the overall increase in efficiency of the TEGs. In this chapter, we will discuss the processing and feasible properties of the different nanocomposite and bulk thermoelectric systems. The physical or chemical methods of nanocomposite/bulk synthesis methods will be discussed, and the theoretical background of intrinsic transport coefficients will be highlighted in this regard. The possibilities of enhancement of the efficiency can be viewed in nanocomposites with special microstructures, which in turn

M. Shalaby
Thermal and Magnetic Lab, Solid State Physics and Accelerators Department, National Center for Radiation Research and Technology, Egyptian Atomic Energy Authority, B.O. Box 29, Nasr City, Cairo, Egypt

S. Hamdy
Cairo Regional Center, Egyptian Metrological Authority (EMA Weather), Cairo, Egypt

I. Islam
Department of Physics, Jamia Milia Islamia, New Delhi, India

K. Kaur
Department of Applied Sciences, Punjab Engineering College (Deemed to be University), Sector 12, Chandigarh 160012, India

A. Nazir
Department of Mechanical Engineering, National Taiwan University of Science and Technology, Taipei 10607, Taiwan

S. A. Khandy (✉)
Department of Physics, National Taiwan University, Taipei, Taiwan

A. E. Shalan et al. (eds.), *Advances in Nanocomposite Materials for Environmental and Energy Harvesting Applications*, Engineering Materials,
https://doi.org/10.1007/978-3-030-94319-6_31

scatter the phonons to minimize thermal conductivity while preserving or increasing the electrical conductivity and the Seebeck coefficient simultaneously. The benefits of these nanocomposites are to enhance ZT by 10–100% and increase the efficiency of thermoelectric devices. In the end, the future perspectives, developments, and challenges of bulk/nanocomposite thermoelectrics are put forward thoroughly.

Abbreviations

TE	Thermoelectric
ZT	Figure of merit
TEGs	Thermoelectric generators
S	Seebeck Coefficient
PGEC	Phonon glass-electron crystal
SEM	Scanning electron Microscope
XRD	X-Ray Diffraction
EDX	Energy Dispersive X-Ray
SAED	Selected area electron diffraction
HRTEM	High-resolution transmission electron microscopy
BF-TEM	Bright field transmission electron microscopy
FWHM	Full-width of at Half Maximum
EDTA	Ethylene diamine tetraacetic disodium salt
PAA	Porous anodic alumina
HOPG	Highly oriented surface of pyrolytic graphite
IGC	Inert-gas condensation
PLD	Pulsed laser deposition
vdW	van der Waals gaps
RGO	Graphene Oxide
DOS	Density of States
DFT	Density functional theory
TMR	Tunneling magnetoresistance

1 Introduction

Economically, current world faces a variety of issues related to energy production and its usage. Global oil supplies and demands continue to rise with the dramatically increase in the prices of Oil [1]. Environmentally, the global apprehensions of the rising impact of greenhouse gases, particularly carbon dioxide and the other carbon products is a prime concern. Politically, the lack of energy supplies will directly influence the poorer countries. Such issues claim the requirement of additional energy harvesting technologies. For the same purpose, several green-energy based modern

vehicle engines, transmissions, and related technologies are in progress to improve the performance of the vehicle transportation.

Still, the absence of one of these crucial problems from the modern-day technologies is quite appealing: most of the energy consumption would still generate unusable heat in the exhaust or cooling systems of the vehicles and other appliances. This waste in the form of heat is equal to two-thirds of the available power reserves of electric plants or the other industrial entities. So, thermoelectric (TE) materials provide a means of transforming this low-grade waste heat energy into electrical energy via the Seebeck effect which was discovered in 1821 [2, 3]. Similarly, a voltage gradient through the junction of a thermoelectric material generates a temperature gradient through the Peltier effect [4]. These categories of materials have been developed into numerous solid-state thermoelectric systems. Due to the significant advantages of thermoelectric harvesting energy systems: no moving parts, long service life, zero emissions, accurate temperature control and the ability to work in the extreme environment [5–7], the expectation of thermoelectric technologies is outstanding, particularly for power production and cooling systems. For power production, energy is collected from waste, environmental, or mechanical/hydraulic supplies and transformed into an exhaustible form — electricity by means of thermoelectric devices [7–10]. Thermoelectric materials are also capable of producing energy via solar radiations to generate a temperature difference throughout the installed thermoelectric materials [11, 12]. Nuclear reactors as well as radioisotope thermoelectric generators are used for propulsion and power supply in spacecrafts [14–17].

In refrigeration modes, air conditioner or micro thermoelectric cooling devices can be mounted in the integrated circuit to resolve the problem of heat dissipation. However flexible thermoelectric materials can be designed in uniforms or clothes of people who are employed in the extreme environment to operate as a wearable climate control system [18].

TE devices efficiency depends on the overall figure of merit (ZT) of the n & p-types thermoelectrics which is defined as [11, 12]:

$$ZT = \frac{S^2 \sigma \ T}{k} = \frac{S^2 T}{\kappa \rho} = \frac{S^2 T}{\rho(\kappa_l + \kappa_e)} \tag{1}$$

where (S) represents the Seebeck coefficient, σ as well as κ are the electrical and thermal conductivities, respectively, T is the absolute temperature in Kelvin, ρ is the electrical resistivity, whereas the thermal conductivity (κ) consists of two parts: lattice thermal conductivity (κ_L) and electronic thermal conductivity (κ_e).

In the power generation mode, the efficiency (ε) can be calculated for both the components of the thermoelectric module (n & p-type) as follows:

$$\varepsilon = \frac{T_h - T_c}{T_h} \frac{\sqrt{1 + ZT} - 1}{\sqrt{1 + ZT} + \frac{T_c}{T_h}} \tag{2}$$

For the cooling/refrigerator devices, the coefficient of performance (COP) is given by:

$$\mathrm{COP} = \frac{T_h}{T_h - T_c} \frac{\sqrt{1+ZT} - \frac{T_c}{T_h}}{\sqrt{1+ZT}+1} \tag{3}$$

where, T_h and T_c are the temperatures of hot and cold surfaces of the TE components, respectively. Also, ZT is occasionally known as the modified dimensionless value of figure of merit of TE devices while considering simultaneously the thermoelectric ability of p-type and n-type components from the materials involved in thermoelectric modules. So ZT may be described as:

$$ZT = \frac{\left(S_p - S_n\right)^2 \breve{T}}{\left(\sqrt{\rho_p \kappa_p} + \sqrt{\rho_n \kappa_n}\right)^2} \tag{4}$$

where, $\breve{T}$ is the average temperature gradient between the hot & cold faces of TE device. The subscripts n and p used to define both the types of the semiconductors p and n-type, respectively, after the geometrical shape optimization for the TE legs is achieved.

Nanostructured PbTe based compounds and alloys have the highest power generation efficiency = 20% with ZT = 2.2 by converting the thermal dissipations to electricity which is 30–40% smaller than the conventional systems [19].

There are limitations in the progression of thermoelectric materials despite the current achievements. The low values of ZT ($\leq$1) of the commercial TE and the efficiency is around 5% as shown in Fig. 1b. So, the competition to make large-scale thermoelectric devices with a high-power efficiency and higher ZT is demanded [20, 21].

To improve the thermoelectric properties of conventional materials, lot more efforts were made, seeking to improve ZT, especially the creation of the nanostructured materials, such as nanocomposite, superlattices, nanowires, and quantum dots. This has been revealed in Fig. 1a, which represents the remarkable progress accomplished for ZT through the past several decades. To promote thermoelectric practical devices and applications, ZT of the synthesized TE must be quite large.

Countless efforts in TE materials research have been evolved in improving the Seebeck coefficient and reducing the thermal conductivity (κ). Numerous reviews have studied the basic theory of nanostructured TE [21, 22] and the developments in bulk materials [23], nanoscale [24–26], or bulk nanostructured TE materials [1, 27, 28]. The impact of interfaces in low dimension TEs such as 1D nanowires or nanotubes [29–33], 2D superlattices (for example, the superlattices of Bi_2Te_3/Sb_2Te_3 and SiGe/Si, the quantum dot superlattices of $PbSe_{0.98}Te_{0.02}$/PbTe) [1, 34–40] and 3D nanograins [29, 41] can improve ZT by scattering the phonons at the interfaces, which in turn diminishes the thermal conductivity. The size of nanoscale materials results in quantum confinement and interface effects as well as significant changes in the density of state of the charge carriers. Quantum confinement impacts are being used to increase ZT by reducing the transport pathways inside the material. Because of the size of the material lower than the mean free path of the phonon, then it is

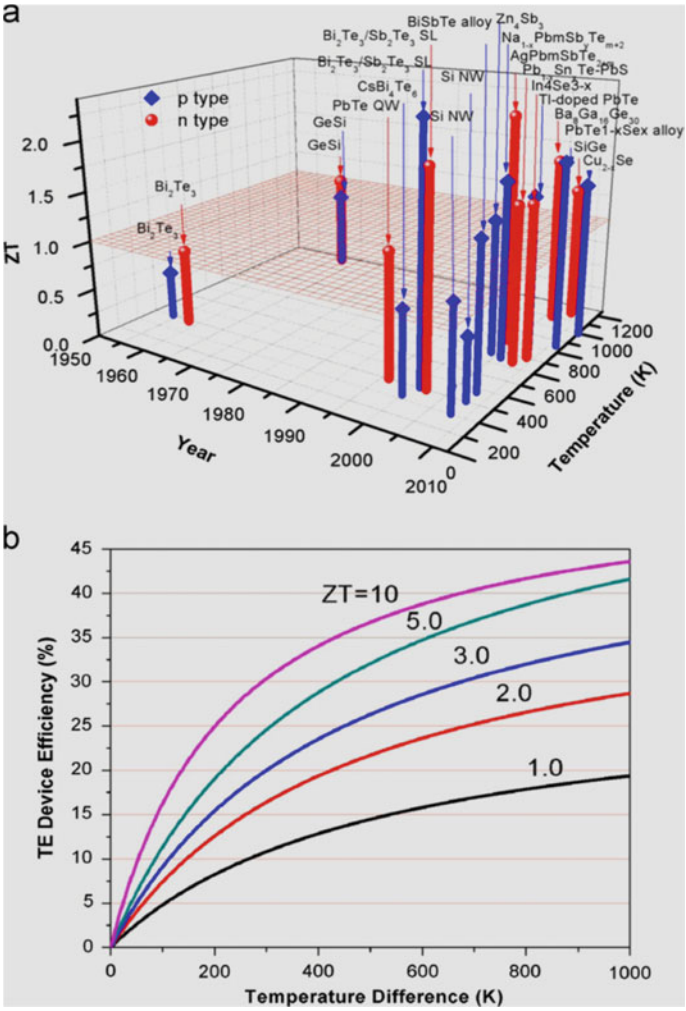

Fig. 1 **a** Figure of merit (ZT) temperature and year dependent data reveals the important achievements of thermoelectric materials taken from Ref. [20] for the available bulk and nano-thermoelectric materials; **b** The energy conversion of TE against ZT at $T_c = 300$ K [20]

restricted and no longer contributes to thermal conductivity and hence decreases reasonably. The main goal is to improve ZT and thermoelectric performance as well [42]. On the other hand, the grain size has a curial effect on thermal conductivity where the reduction in the grain size may decrease it to 1/3, at the same time Seebeck coefficient S and the electrical conductivity are not affected compared to the single crystal materials [43]. Thus, nanostructured TE's have a great impact on ZT: In Bi_2Te_3 nanograins ZT increased by 40%, in case of n-type semiconductor Si-Ge alloys ZT reduced by 40% [44], where P-type Si-Ge alloys 90% increase in ZT [45],

50% higher for both p-type half-Heuslers [46] and In_4Se_{3-x} (n-type) [47], and by around 4 times larger in MgAgSb composites equal to 1.4 [48].

1.1 Nanocomposites and ZT Improvements

To maximize ZT, lot more attempts have been made and its value stayed stagnant around 1 over 50 years for all the temperature range. So, it became important to make advancements in the usage of new materials like alloys, thin films, bulk materials …etc. In the 1990s, the most common two analogous methods were anticipated for ZT augmentation of thermoelectric materials: i) the first approach was based on new categories of superior bulk materials [49–51] called as ratters in which the crystal structures contain weakly bound atoms or molecules with large vibrational amplitudes at partially filled structural sites acting as effective phonon scattering centers. The concept of phonon glass-electron crystal (PGEC) formulated by Glen Slack [52] has also been beneficial in guiding efforts in this direction. Material structures such as skutterudites (e.g., $CoSb_3$) [53–55], Clathrates (e.g., $Ba_8Ga_{16}Ge_{30}$) [56–58] and Zintl phases [60] fall within this group. ii) The second approach involves the use of low-dimensional materials (including quantum structures-wells/wires/dots) [60, 61] which would end up in the advancement of ZT via two strategies: i) nanoscale characteristics that endorse confinement effects resulting in an increase in the power factor $S^2\sigma$, and (ii) the existence of several interfaces in nanocrystals to increase phonon scattering rather than their counterparts (electrons) and thus reduce thermal conductivity without altering the electrical conductivity [29, 62].

The added value of this approach to the present research guidelines promotes the special design and synthesizing of the nanocomposite materials for improved TE performance. The three parameters S, σ and κ for the 3D-bulk materials are dependent and connected in somehow that restricted to controlling them indecently to enhance the overall ZT of the material. That is because, for example, S increase (by reducing carrier concentration) consequences in a frequent reduction in σ, where any increase in σ usually produce a rise in the electronic part of κ, owing to the Wiedemann–Franz relation. Conversely, if the dimensions of the material are reduced, the nano-scale lengths manage the properties of the material in the form of new effective variable. It is also conceivable to generate vivid changes in the density of states, permitting new prospects or chances to make S, σ, and κ vary in a quasi-independent fashion. One of the other effects of small dimensionality (e.g., less than ~100) is the appearance of quantum-confinement effects with respect to the decrease in number density of atoms in any of the 3D (x, y, or z) directions.

Also, the tunable dimensionality from 3D crystals to 2D (quantum wells) or to 1D (quantum wires) and lastly to 0D (quantum dots) leads to the new material properties like metal–semiconductor transition (as introduced for Bi nanowire composites) accomplish the new projections to alter S, σ, and κ individually. In addition, the

existence of various interfaces, scattering the phonons more efficiently than the electrons and the energy barriers filter the low-energy electrons, making the nano-sized materials appropriate for TE applications and devices with enhanced ZT's [29].

From the last few decades, theoreticians and experimentalists by wide use of quantum wells [61] and quantum wires [62] demonstrate the improvement of ZT. In this respect, PbTe superlattices grown by Harman et al. achieved a high ZT of ~1.7 (at 300 K) and 3.5 (at 570 K) [64]. Contrarily, the lattice thermal conductivity κ_l in the superlattices reduced to ~0.33 W/mK, being 6 times less than bulk PbTe (~2.4 W/mK). Further, the intensive experiments demonstrated that the ZT is actually increased by reducing the thermal conductivity and the augmentation in Seebeck coefficient makes no sense. Also, the exhibition of band alignment in these low dimensional materials (in Na-doped PbTeSe compound) elevates the ZT to 1.8.

p-type superlattices of Bi_2Te_3- Sb_2Te_3 have been utilized by Venkatasubramanian et al. using the molecular beam epitaxy technique [36]. Now it became obvious that it is possible to improve the ZT of materials much beyond 1 by designing the thin films as proposed by the early works or by nanostructures. Besides, nanostructuring effectively raised ZT for Bi_2Te_3, PbTe, and GeSe to over 1 near room temperature [20, 45]. However, SnTe nanocomposites are lead-free and ecofriendly thermoelectrics with ZT $\geq$ 1.2 due to the exhibition of band convergence and introduction of nanoprecipitates [69–73]. On the other hand, SnSe nanocomposites and its doped forms (Na-doped materials) achieved ZT $\approx$ 2.6 attracted the attention of the researchers [75–78].

1.2 The Basic Theory for ZT Enhancement

As mentioned previously, high ZT material/compound needs to have some features such as a high S, low carrier concentrations which existed in the semiconductors or insulators. However, a low electrical resistivity or a high electrical conductivity in metals is due to the plenty of carriers. So, the thermoelectric power factor could be maximized somewhere between the carrier concentrations of metals and semiconductors, as shown in Fig. 2 [25]. Particularly, the mathematical relation of Seebeck coefficient and carriers concentrations is given by:

$$S = \frac{8\pi^2 K_B^2}{3eh^2} m^* T \left(\frac{\pi}{3n}\right)^{2/3} \tag{5}$$

where k_B is the Boltzmann constant, e is the charge carrier, h is Planck's constant, m^* is the effective mass of the charge carrier, and n is the carrier concentration. The relationship between electrical conductivity and carrier concentration can be defined as

$$\sigma = ne\mu \tag{6}$$

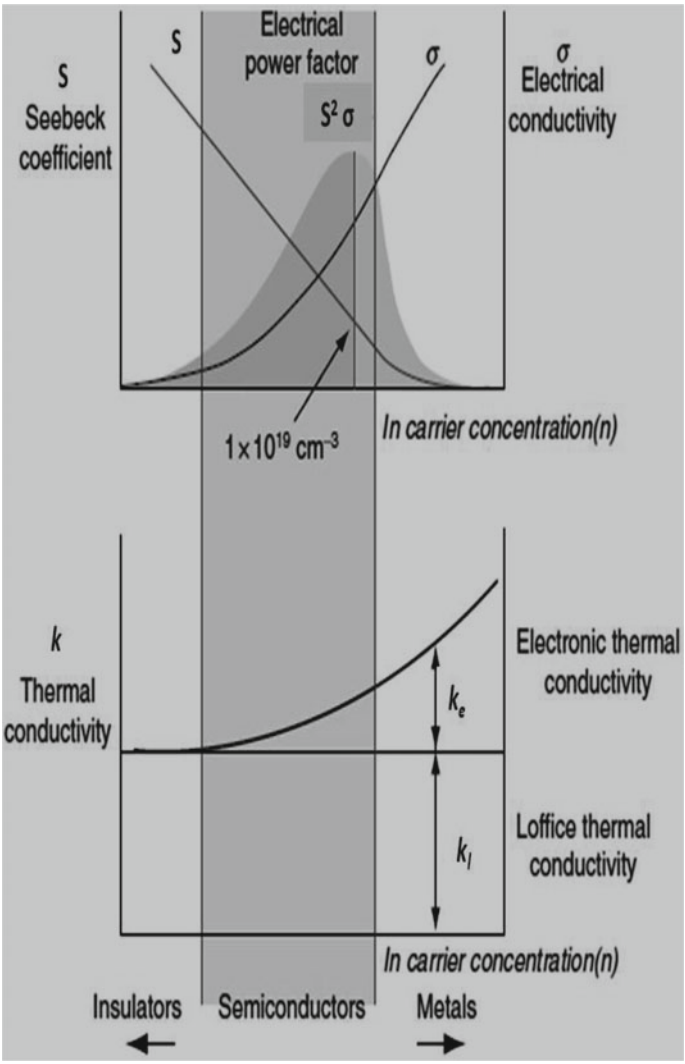

Fig. 2 The Seebeck coefficient(S), the electrical conductivity(s), the power factor ($S^2\sigma$), the electronic thermal conductivity (κ_e), and the lattice (κ_l) thermal conductivity variations on the charge carrier concentration n, for a bulk material

where, μ is the mobility of the carrier. Usually, the good TE's are the heavily doped semiconductor materials that have carrier concentrations up to 10^{19}–10^{21} cm^{-3} [25]. A single type of carrier (n-type or p-type) is preferable to maximize the Seebeck coefficient, because the mixed n-type/p-type charge carriers would produce the opposite Seebeck effect, lowering the thermopower. To accomplish a single type of carrier, it is crucial to choose materials with proper energy band gaps and fitted doping,

wherein n-type and p-type ranges can be well defined. Therefore, efficient TE's are semiconductors (heavily doped) with energy band gap lower than 1 eV to achieve both single carrier type as well as sufficiently high carrier mobility. The decoupling of both the thermal and electronic terms control the ZT and hence, counting the electrical conductivity and Seebeck coefficient has been the key methodology to raise ZT.

The low thermal conductivity is also needed for more efficient TE materials. Whereas the two parts of the thermal conductivity are: κ_l, that represents the transported heat from phonons itinerant through the crystal lattice and κ_e results from the heat carried by the charge carriers (such as electrons or holes) traveling through the crystal lattice. According to the Wiedemann–Franz Law

$$\kappa_e = L\sigma T \tag{7}$$

where L is the Lorenz number, as shown in Fig. 2, It is found that the electronic thermal conductivity (κ_e) is proportional to the electrical conductivity (σ). Consequently, to diminish the electronic part of the thermal conductivity for TEs is not always the best option, while it will inversely impinge on the electrical conductivity and has slight or no enhancement of ZT. Lattice thermal conductivity can be defined by

$$\kappa_l = {}^1\!/_3\left(C_\upsilon \upsilon_s \lambda_{ph}\right) \tag{8}$$

where C_υ is heat capacity, υ_s is the velocity of sound, and λ_{ph} is mean free path of the phonon. It can be concluded that lattice thermal conductivity is the electronic structure independent parameter so that the improvement of ZT can be obtained by lattice thermal conductivity minimization.

The operational TE materials with a high ZT are the PGEC being the best practicable material with complex crystal structures, which contains voids (vacancies) and rattlers where the heavy element atoms, sited in the voids, could act as scattering centers to the phonons and hence lowering the lattice thermal conductivity (κ_l) notably. Also, the nanoscale materials were recommended to achieve large ZT because the structural arrangement of nanostructured materials foster the density of states (DOS) nearby Fermi level by quantum confinement effect and upsurge the thermopower, which grants a technique to decouple thermopower and electrical conductivity [26, 29].

Furthermore, nanostructuring is used to establish a wide density of interfaces wherein phonons can be more effectively and preferentially scattered over a large mean free path range than electrons, as demonstrated in Fig. 3. Thus, significantly lowers the thermal conductivity of the lattice while retaining carrier mobility and electronic conductivity. This can be accomplished by designing the nanostructures with reducing dimensions less than the mean free path of the phonons, but still longer than those of the charge carriers.

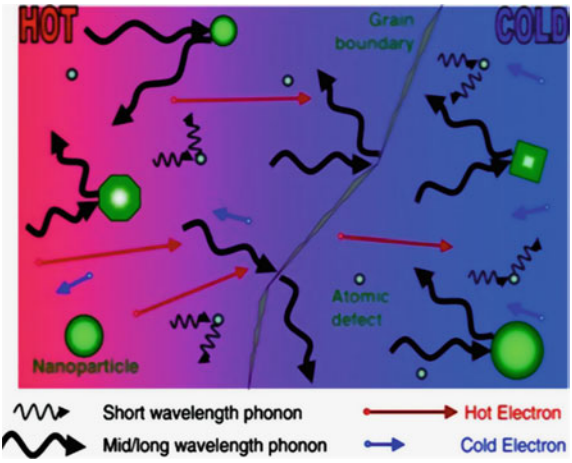

Fig. 3 Illustration of phonons scattering mechanisms and electronic transport of hot and cold electrons within TE materials [20]

1.3 Thermoelectric Nano-Structuring Methodologies

TE nanocomposites are typically produced by bottom-up strategies where the nanoparticles are fabricated first and then compacted into nanostructured bulk materials. The thermoelectric nanoparticles can be synthesized by several bottom-up methods (such as hydrothermal techniques, wet chemical reaction, and melt spinning method), and/or top-down methodologies (such as ball-milling). Amongst these approaches, ball-milling of high-energy type is an efficient and dominant processing strategy for nanoparticles in short times especially for the production of large quantities. Here the common strategies of ball-milling approach for nanoparticle fabrications will be discussed and reviewed.

1.3.1 Ball-Milles/Mechanical Attrition

Ball-Milling or Mechanical attritions are classified as one of the best common synthesis techniques for nanocomposites from bulk raw materials because they are more convenient, demand minimum specifications, less requirements of advanced equipments and flexibility in terms of the number of various categories of solid materials can be achieved by using this method.

Micro-sized TE particles were traditionally prepared by an old method of ball-milling in early 60s. It was found that the gradual reduction in the size of TE particles reached to micrometers in low energy environments. The final product of TE particles were packed in and ZTs were found to be enhanced slightly. SiGe composites have been prepared and used later in radioisotope thermoelectric generators (TEG).

The progress of the high-energy ball-milling technique was launched in the 70s and the mid of 80s to carry out the synthesis of variety of materials, including

superalloys, homogeneous composition ball-milled powders, amorphous alloys and severely deformed alloys. Till date, numerous types of high-energy ball mills were utilized to produce nanocomposites, for example, the shaker mills, the planetary mills, or the attrition mills.

The most popular types of ball mills differ in their specifications and the mechanisms used in the grinding media as the products of many companies. Figure 4 shows SPEX 8000 mixer/mill and the typical planetary ball mill.

Also, Table 1 describes the three types of high-energy ball mills with the calculations of ball velocities, the usage Kinetic energies for each impact; power and shock frequencies are reported as well. For instance, the ball mills from high-energy type have a high impact velocities as well as the impact frequencies especially for producing nanocrystalline materials for different grinding media. The used time for milling process relies on the energy and the frequency of impact of the mill balls. For instance, Just 20 min SPEX shaker milling is the counterpart to nearly 20 h of milling in the other types of low-energy mills like Invicat BX920/2. Also, it was known that the process of milling within SPEX shaker in few minutes is equivalent to hours in attritors and some days in a traditional low-energy mill. Although the usage of this technique in preparing TE materials is common but, there are some challenges such as the effectiveness of the reduction of the particle size is 0.1% in the traditional ball

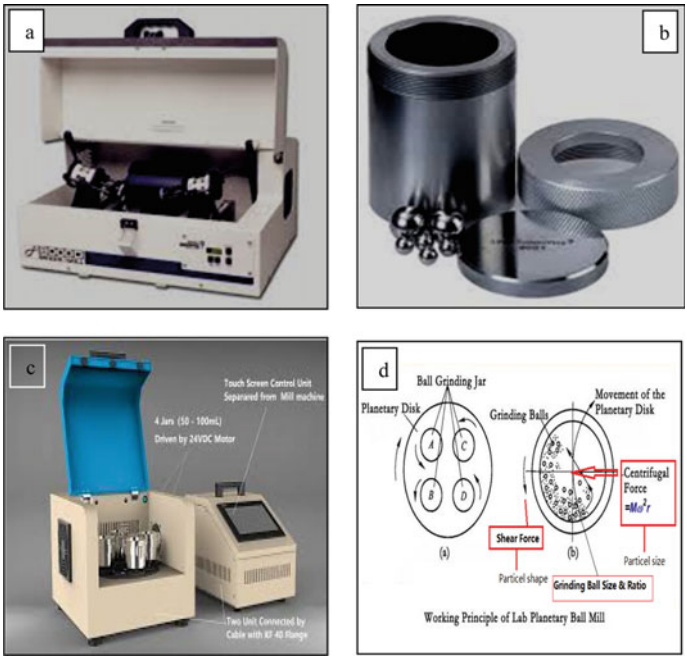

Fig. 4 **a** SPEX 8000 mixer/mill, **b** the vial and the balls, **c** planetary ball mill, and **d** the principle of the working of the planetary ball mill

Table 1 Three types of high-energy ball mills parameters

Parameter	Attritors	Shaker		Planetary ball mills		
		O[a]	SPEX mill	P5[a]	G7[a]	G5[a]
Velocity of Balls (m/s)	0–0.8	0.14–0.24	<3.9	2.5–4.0	0.24–6.58	0.28–11.24
Power (W/g/ball or rod)	<0.001	0.005–0.14	<0.24	0.01–0.8	0–0.56	0–1.604
Kinetic energy (10–3 J/hit)	<10	3–30	<120	10–400	0.4–303.2	0.53–884
Shock frequency (Hz)	>1000	15–50	200	≈100	5.0–92.4	4.5–90.7
Atmosphere	Varied	Varied	Vacuum, gases	Varied	Varied	Varied
Capacity	Different capacities	Different capacities	0.2–10 gm	Different capacities	12 and 45 ml	Different capacities

[a] FRITSCH Pulverisette

mills and <1% in high-energy ball milling. The balls may cause some contaminations in the product due to the difficulty in cleaning the balls. The destruction of the long-range ordered structure or even amorphous materials of different nanoparticles could be generated during this process.

1.3.2 Ball Milling/Attritions TE Nanocomposites

Milling or Mechanical attrition used in fabricating TE nanocrystals by transferring the structural decomposition of the raw materials of coarse grains into finer or smaller structures due to the plastic deformation achieved at room temperature. This procedure can be accomplished by any type of Ball milling route such as high-energy mills, the type of centrifugal, including vibratory mills types, or even by low energy tumbling mills. The ranging of the nanoparticle size achieved by attritors, horizontal mills or even the vibratory mills are in the range from 150 till 5–10 nm. The sensitivity of this procedure to the contamination and other infections from the milling environment urges the usage of a nicely atmospheric control and is vital in preserving the material purity, especially to avoid oxidation. Therefore, Ar and N gases are the most popular atmospheric gases employed in the fabrication of thermoelectrics. Another method for producing new phases in nanoscale is Mechanical alloying but it usually needs double-time more than the ordinary milling process to reach the nanoscale requirements.

Since 2008, mechanical attrition and high energy ball milling techniques have been employed widely in the fabrication of Fe-Si nanopowders, Si-Ge based alloys

[45], PbTe, PbSbTe alloys, SnTe, Bi_2S_3, BiSbTe alloys [97], MgSiSn, $CoSb_3$, Bi_2Te_3 nanoparticles [45, 102, 103], Zn_4Sb_3, MgAgSb, $AgPb_{18}SbSe_{20}$ (LAST), $YbAgCu_4$, half-Heuslers, In_4Se_3, skutterudites [113–115], including $La_{3-x}Te_4$ which display a challenge to be fabricated by the conventional approaches.

Table 2 records some conventional TE nanoparticles fabricated by the ball-milling route. The obtained crystallite sizes from ball-milling, power factor (PF), and the figure of merit (ZT) are also tabulated. Some of the TE nanoparticles were achieved by the mechanical milling technique where other TE's were produced through the mechanical alloying route.

Both of single-crystalline nanoparticles (such as Bi_2Te_3 and Zn_4Sb_3 nanoparticles with particle size 20 nm) as well as polycrystalline nanopowders can be obtained by

Table 2 Some conventional TE nanoparticles fabricated by ball-milling route

TE materials	Size	PF	Max ZT
$Si_{95}Ge_5$	10–30 nm	40	0.95
$Si_{80}Ge_{20}$	7 nm	N/A	1.5
$Al_{0.05}La_{0.5}Co_4Sb_{12}$	N/A	40.2	1.36
$Ce_{0.8}Fe_3CoSb_{12}$	94	21.6	0.68
$Ce_{0.5}Yb_{0.5}Fe_{3.25}Co_{0.75}Sb_{12}$	104	22	0.93
$Pb_{0.95}Ce_{0.05}Te$	N/A	10	0.88
$(Bi,Sb)_2Te_3$	5–50 nm	N/A	1.4
$(Bi_2Te_3)_{0.95}$–$(Bi_2\ Se_3)_{0.05}$	N/A	N/A	1.7×10^{-3}
Cu_2Te	<10 nm	N/A	N/A
Zn_4Sb_3	5–20 nm	N/A	1.2
$Bi_{100-x}Sb_x$	N/A	N/A	1.4×10^{-3}
$Ca_5Al_{1.9}Mn_{0.1}Sb_6$	1–10 μm	4.2	0.4
$Ca_{4.8}Zn_{0.2}Al_{1.8}Sb_6$	1 μm	3.75	0.4
$Ca_{2.94}Na_{0.06}AlSb_3$	50 μm	3.76	0.78
$Ca_5Ga_{1.9}Zn_{0.1}Sb_6$	1–5 μm	0.546	0.35
$Yb_{0.99}Zn_2Sb_2$	N/A	19.6	0.85
$Sr_5In_{1.9}Zn_{0.1}Sb_6$	N/A	3.64	0.4
$Mg_{3.2}Sb_{1.5}Bi_{0.49}Te_{0.01}$	N/A	13	1.5
n-type Mg_2Ge	N/A	10.8	0.32
Sb doped Mg_2Ge	N/A	N/A	0.2
Bi-doped $Mg_2Si_{0.6}Sn_{0.4}$	>10 μm	N/A	1.36
V- doped$SrTiO_3$	1.4–3.5 μm	4.76	0.084
Y-doped $SrTiO_3$	N/A	6.64	0.18
$ZnO/Bi_2Te_{2.7}Se_{0.3}$	>20 μm	22	~1.3
$Ca_{0.96}Gd_{0.04}MnO_{3-\delta}$	110 nm	3.56	0.14

the mechanical milling process. TE ingots are prepared and then exposed to grinding process via ball-milling to fabricate TE nanocomposites which have finally the same chemical compositions. The ductile TE materials like half-Heuslers fragments can be grinded down to achieve polycrystalline nanoparticles by high-energy milling. Besides, Fig. 5 (a, b) illustrates bright-field transmission electron microscopic (BF-TEM) pictures of ball-milled Bi_2Te_3 and Zn_4Sb_3 nanosized particles, respectively. Figure 5c illustrates the images of TEM of ductile half- Heusler particles with nano-crystallites ranging from 50–100 nm.

It should be noted that the previous research pointed out that the speed and the time of milling are notably influencing on the achieved the crystal size of nanoparticles. Figure 6 illustrates how the crystalline size of Cu_2Te ball-milled nanoparticles changes at various ball-milling times. The nanoparticles of Cu_2Te were basically elemental powders of Cu and Te mechanically alloyed via the planetary milling at the room temperature. It was studied that the grain size estimated from XRD diffractograms decreased drastically at first while changing the time of ball-milling and then finally becomes constant with milling time.

The better and powerful technique used to identify the nanoparticle size accurately is TEM but also could be characterized by SEM where it usually gives the geometrical size not the crystalline size of the nanoparticles. Also, XRD may give better information for the nanoparticle grain size or crystalline size of any range by observing the changes in the peak positions and cell parameters. The grain size can be calculated utilizing the Rietveld method or by the traditional methods from Scherrer and Williamson–Hall equations to calculate both the grain size and the strain from The Full-width at Half Maximum (FWHM).

Also, the modified Scherrer equation is given below [43]:

$$B = \frac{0.9\lambda}{d \cos \theta} + \eta \tan \theta \tag{9}$$

The used parameters were d, λ, η that represent the crystallite size, the used wavelength of XRD beam and the strain, respectively, also B is the width at FWHM, and θ is the Bragg's angle. Thus, the procedure to calculate d and η, first plot B cos θ against sinθ, from the obtained straight line, the slope is equal to η and $0.9 = \lambda/d$ is the intercept. So, d as well as η can be experimentally calculated from XRD diffractograms.

It should be noted that the agglomeration of the nanoparticles to compose several smaller particles usually happens significantly with ball–milled processing. Besides, each particle may perhaps consist of quite a few sub-particles identified as consistently diffracting grains/domains. So, it takes into consideration the careful determination of precise crystalline size/grain size from SEM techniques.

One of the observations of the obtained nanoparticles from ball-milling processing is the production of high density grain boundaries in TE nanoparticles. The various defects especially the grain boundaries can strongly scatter the phonons more than the other charge carriers that reduce the thermal conductivity and improve the ZT of

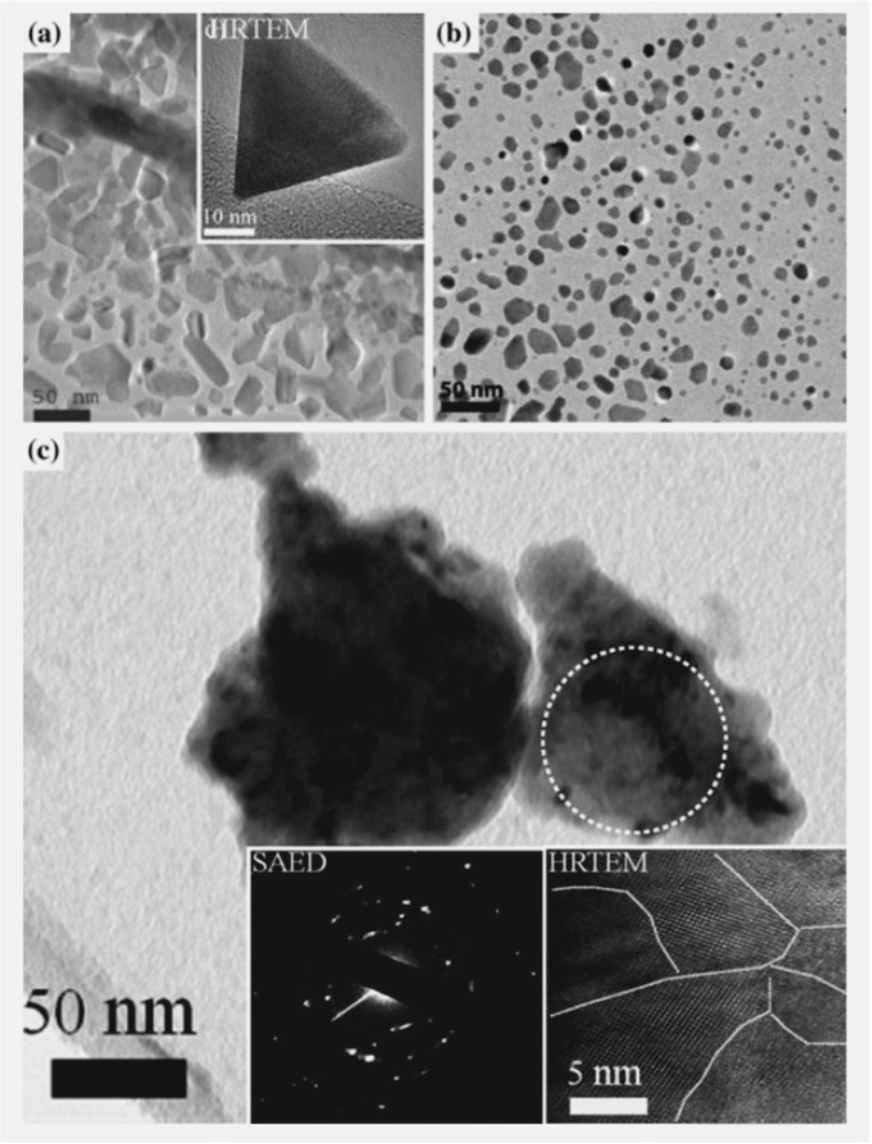

Fig. 5 The ball-milled nanosized particles of images for: **a** p-type Bi_2Te_3. **b** Zn_4Sb_3. **c** Half-Heuslers. The circle region is represented by SAED and HRTEM the right view

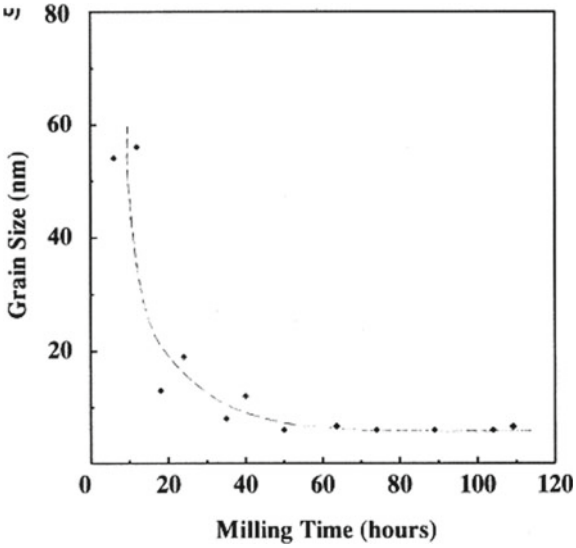

Fig. 6 Crystalline size of mechanical alloyed Cu_2Te nanoparticles

the nanocomposites. The TE nanocomposite fabrication methods will be discussed in the next section.

1.3.3 Wet Chemistry Synthesis

One of the outstanding techniques for nanocomposite fabrications in different shapes is the wet chemistry procedure. The solvo-thermal method (counting hydrothermal route) fabricates the nanostructures using the appropriate solvents of inorganic powders and precursors above the critical point/temperature of the solvent depending upon the self-formed pressures in an autoclave after the crystallization of the dissolved materials from the solution. In Comparison to other preparation techniques carried out at atmospheric pressure, increase of both the reaction temperature and the time in the solvothermal method may accelerate the crystal growth of the prepared compounds which come up with a smaller particle size distributions and improved crystallinity. One more benefit from this technique is that the nanocrystals may have different morphologies and shapes like, nanopowders, nanorods, nanoplates, multi-lateral nanosheets or nanoparticles, sheet-rods, etc. Also, the solubility of most of the materials in the different solvents by heat or pressure beyond the critical point makes this technique promising for synthesizing nanocomposites of numerous solid materials.

Hydrothermal method was used widely in the preparation of nanostructured TE materials such as Bi_2Te_3 based compounds, doped-Sb_2Te_3, PbX (X = S, Se, Te), $CoSb_3$, half-Heuslers, and $Cu_2CdSnSe_4$ etc. On the other hand, the tuning in the

preparation conditions like temperature, PH, time, the usage of different surfactants is the powerful tool in the fabrication of nanostructure particles within different shapes throughout an anisotropic growth process. Figure 5 illustrates different nanostructured forms of Bi_2X_3 (X = Se,Te), and Sb_2Te_3 that have the same layered rhombohedral crystal structure with D^5_{3d} (R3m) space group. The most common structure synthesized from the solvothermal technique is the hexagonal nanoplates where Fig. 7a shows a typical hexagonal nano-plate of Sb_2Te_3. Here, the effect of the surfactant ethylenediaminetetraacetic disodium salt (EDTA) was added to the precursors through the usage of the hydrothermal processing. Bi_2Te_3 nano-capsules were obtained from polyhedral shell formations as illustrated in Fig. 7b. Contrarily, with the support of some polymer additive, nanowires can be developed by employing the same solvothermal process. Yu et al. articulated a synthesis technique of Te nanowires from the high-temperature decomposition of $TeCl_4$ in polydecene by the assistance of trioctyphosphine oxide in the form of surfactant. Tellurium nanowires act as a guide for the Bi_2Te_3 nanowire productions by making the reaction with $Bi[N(SiMe_3)_2]_3$ or $BiPh_3$. Bi_2Te_3 nanowires are displayed in Fig. 7c. PbTe is one

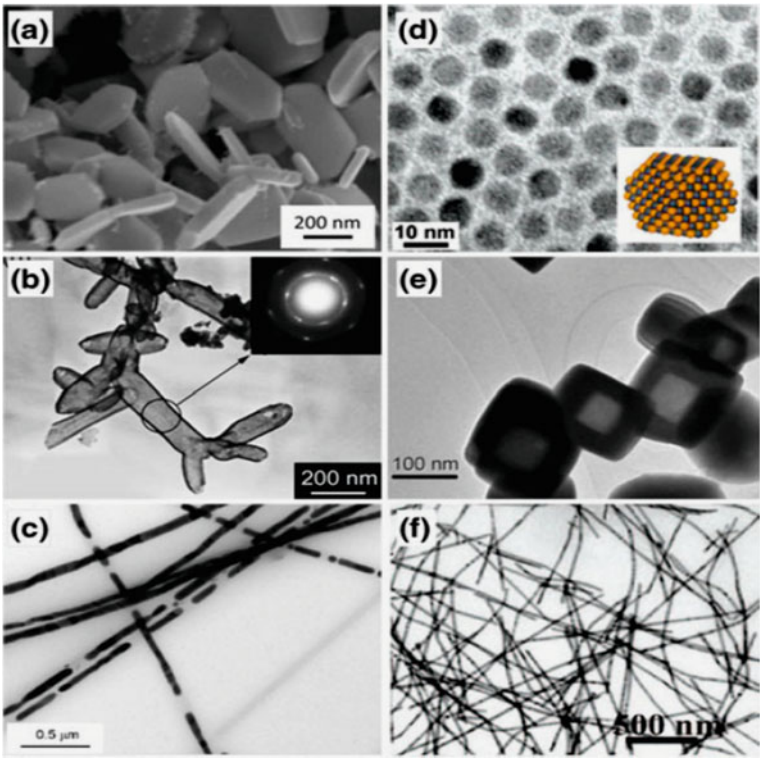

Fig. 7 Bi_2Te_3 TEM images with different nanoparticles shape: **a** nanoplates, **b** nanocapsules, **c** nanowires, and **d** represents PbTe nanoparticles; **e** nanoboxes, **f** and nanowires, the Figures were adapted from [157, 159]

of the classic TE materials but it has a cubic lattice structure. There are numerous chemical method synthesis procedures to grow the nanocomposites of PbTe that have been extensively studied. Figures 7d–f represents the different nanostructured forms, cuboctahedral nanoparticles, nanoboxes, and nanowires respectively, where they have been obtained by the assistance of solvothermal approaches. Chemical routes show well-defined nano shapes, for each particle and were supposed to have fewer defects than those obtained from the ball-milled technique and also have a high mobility carrier.

The final product materials bulk prepared from the different chemical routes may have different atomic defects at the grain boundaries. Small amounts of light elements, such as C, N, and O are residing at these boundaries contribute in producing little thermal conductivity.

Conversely, it is very unfavorable to the transportation of charge carriers in some systems. For instance, the carbons as well as the oxygen atoms, have been confirmed experimentally to have a considerable reduction in the mobility carriers of p-type Bi-Te system where oxygen atoms can be easily introduced during the production of Bi_2Te_3 nanoparticles via the chemical approaches. This makes the carrier concentrations to improve and the Seebeck coefficient (S) to reduce in n-type Bi-Te systems.

So far, the mechanism to transform the high-quality nanoparticles prepared by chemical routes with extraordinary characteristics for TE application is still a challenge and not an easy task.

1.3.4 Electrochemical Deposition

One of facile and effective methods to obtain nanostructured metal alloys is the electrochemical deposition technique [161]. First time the high-quality Bi_2Te_3 nanowires were obtained by Stacy's and co-researchers via the template-assisted (porous anodic alumina (PAA)) electrodeposition processing. This approach has the promotion in fabrication of nanowire arrays, such as doped n-type Bi_2Te_3, doped p-type Bi_2Te_3, Sb_2Te_3, $CoSb_3$, PbTe based compounds, etc. [164, 165]. This technique has an advantage in controlling the diameter and the length of the nanowires. The obtained diameter was ranging from 20–300 nm for as-prepared nanowires and is pore size dependent, whereas the length is directly proportional to electrodeposition time.

Also, the composition of the alloys is controlled by changing the electrolyte solution concentration. The arrays of nanowire orientations can be adjusted by varying the deposition potentials or via pulsed electrodeposition procedure. The electroplating can be used to develop a uniform growth of the arrays at low temperatures. Moreover, novel hollow TE nanocrystals can be realized within some special electrodeposition conditions. Li's group articulated the successful production of nanotube arrays of Bi. Zhu's et al. synthesized Bi_2Te_3 and its derived nanotubes arrays. In contrast, 1D chime like Bi-Sb nanocomposites were obtained by Li et al. without the support of

templates. Xiao et al. exemplified the PbTe cube shapes to be instantly deposited on a gold substrate with the polycrystalline structure. By the assistance of the cyclic electrodeposition or so-called stripping method, notable yields of long polycrystalline nanowires from Bi-Te were deposited wisely on the highly oriented surface of pyrolytic graphite (HOPG).

Heterostructures nano-materials can also be obtained by using the electrodeposition technique. The deposition potential is a crucial parameter when template-assisted pulsed electrodeposition is used in the preparation of TE materials. Wang and his group presented a detailed investigation of Bi-Sb–Te and efficiently controlled the growth of Bi_2Te_3/Sb nanosystems in a very low time. The minimum period of as-synthesized Bi_2Te_3/Sb heterostructures achieved low dimensions nearby 10 nm as depicted in (Fig. 8). On the other hand, they also prepared Bi_2Te_3/Te heterostructure nanowire arrays by using the precipitation method to obtain a nano-confined structure

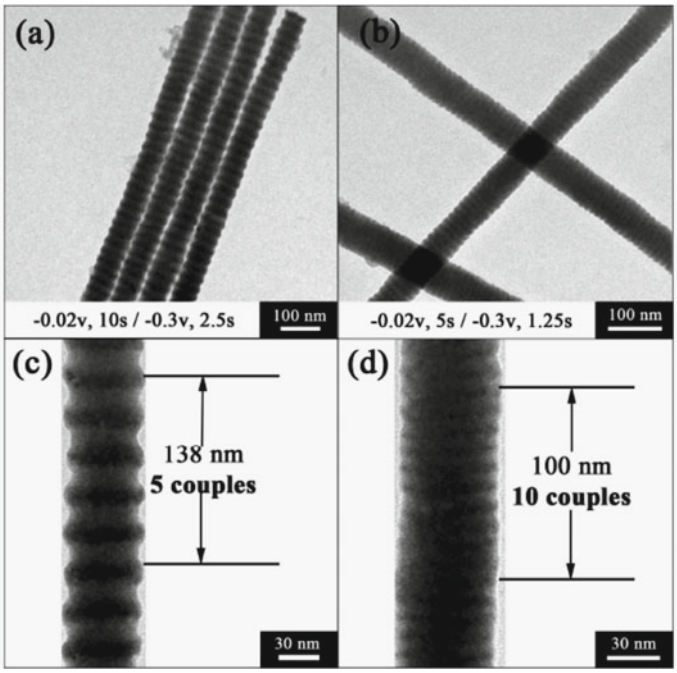

Fig. 8 **a** and **b** illustrate the TEM images of multilayered Bi_2Te_3/Sb nanowires deposited in various conditions where **c** and **d** represent the corresponding highly magnified TEM images

1.3.5 Inert Gas Condensation Method

The inert-gas condensation (IGC) processing contains some important parameters such as evaporating, sputtering, or ablating materials that are inside of an evacuated chamber kept at a pressure of about 10^{-8} mbar and a low-pressure inert gas like helium is back-filled to the machine.

This route depends on the collision between the material atoms and the gas atoms inside the evacuated chamber, where they are losing their kinetic energy (K.E) and thereby finally condense in the form of small particles. The inert gas condensation approach generates equiaxed crystallites. The crystallite size of the powder obtained from this method ranges in nanometer scale and the size distribution is reduced. The inert gas pressure as well as the temperature, the evaporation/the sputtering or the ablation rate, and the gas type play a vital role in the crystal size formations.

IGC is an effective tool used today for obtaining experimental amounts of metallic nanocrystal and intermetallic powders as well. The best feature of this technique is the ability to generate non-agglomerated nano-powders, especially at low temperatures. First, an evaporative source produces the powder particles, and then the product is convectively carried out and collected on a cold substrate. The nanoparticles acquire in a thermalizing area just above the evaporative source, because of the interactions between the hot vapor species and the much colder inert gas atoms in the chamber typically at 1–20 mbar pressure. Lately, this technique has been accommodated for fabricating Si-Ge nanocomposites. Also, Magnetite (Fe_2O_3) thin films are promising TE's used for thermoelectric applications that were deposited on the surface of SiO_2/Si substrates using Pulsed laser deposition PLD at 300 °C.

1.3.6 Nanoprecipitation/Phase Separation Approach

The technique of nanoprecipitation is a successful solid-state route in the process of the fabrication of nanostructured bulk materials throughout the nano-inclusion. For example, PbTe-based nanocrystals including $AgPb_mSbTe_{2+m}$ (LAST-m) can be simply produced by this approach [184–188]. Throughout the cooling procedure of the molten material, nano-inclusions are obtained inside the matrix by phase separation or spinodal decomposition. Nevertheless, it is hard to manipulate the carriers from sample to sample due to the striving nature of the system and its phase diagram. So, the accuracy in controlling the temperature is a crucial point in this method of preparation. This technique is having the ability to fabricate a nanoscale lamellae structure. For systems like Sb_2Te_3/PbTe and $Pb_2Sb_6Te_{11}$, the decomposing of the phase near the eutectic happened in PbTe and Sb_2Te_3, where lamellae of nanostructured Sb_2Te_3 and PbTe are produced during the fast cooling process. The benefit of this approach is the one-stage method where nanoscale attachments or lamellae are produced simply by thermal treatment. Also, this technique is favorable for electronic transport because it presents coherent or semi-coherent interfaces.

Other chalcogenide materials not related to this shortcoming method are still being surveyed because it is outstanding in situ approach to prepare TE nanocomposites.

1.3.7 Spark Erosion Technique

One of the adjusted methods to fabricate TE nanoparticles with a particularly high synthesis yield is the spark erosion technique. It was initiated for producing fine powders of metals, alloys, and compositions on a micro-scale. Figure 9 schematically illustrates the components of this technique. The two electrodes in the left diagram are immersed into a dielectric liquid connected to a pulsed power supply on the upper side of the cell.

To generate a spark the applied field strength needs to be adequately high in the gap. The initiated spark may be generated from the breakdown inside the dielectric fluid, as described in the reaction zone in the magnified graph on the right side of Fig. 9. If the electric field is proposed to be improved to a high level, electrons can be released substantially and emitted from the cathode. These electrons plus the others in the gap collect the energy from the electric field, ionize the molecules of the dielectric fluid, and produce more ionized electrons and ions. In almost 10 ns of the electric field application, a very small diameter from plasma is established and temperature must be high (it may exceed 10,000 K).

The plasma column has a high temperature so it must be enveloped by a sheath of vaporized dielectric fluid which is controlled by the assistance of incompressible liquid as shown in Fig. 9. Besides, the kinetic energy states are transferred to the electrons and the ions into the anode and the cathode, respectively, which improves the temperature at the electrodes. Due to the much higher electron mobility than that of the ions; short spark times favor anode wear. Consequently, the applied pressure by the plasma channel enhances locally on the electrodes, the temperature of these heated local sections is increased higher than that of the boiling point of the metal. A quick reduction of the pressure takes place at the end of the voltage pulse producing a spark falls, the superheated sections may be boiled violently producing molten droplets and vapor also inside the dielectric liquid as well as liquid nitrogen (N), liquid argon (Ar), water, etc. The erosion process may be enhanced by the violent boiling of superheated regions or other mechanisms. For thermoelectric materials, spark erosion was used to fabricate Bi-Te nano-grained alloys by two different: (1) the development

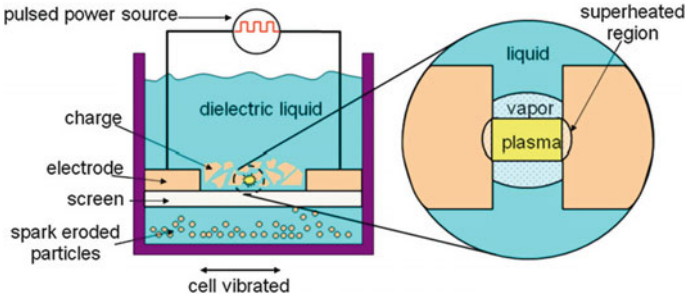

Fig. 9 Schematic diagram of the spark erosion technique for obtaining nanoparticles of a TE alloy

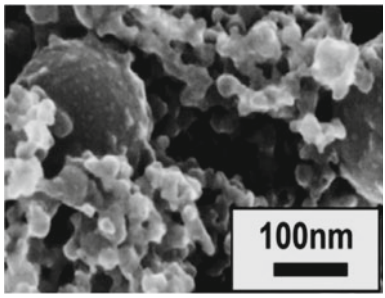

Fig. 10 SEM image Bi-Sb–Te nanoparticles prepared by spark erosion

of nanoparticles ranging from 20–30 in nm size, and (2) the establishment of micro-sized particles ranging from (0.1–10 m) containing nano-grains as illustrated in Fig. 8.

Generally, the spark erosion method often produces a mixture of these two types of particles. For example, the spark-eroded nanocomposite $Bi_{0.5}Sb_{1.5}Te_3$ exhibits a high ZT value of 1.36 at 360 and the ZT values are analogous to those alloys synthesized by other top-down approaches. Spark erosion has a lot of benefits and advantages, especially the production of nano-particles, the rate of processing efficiency, and the scale-up potential K (see Fig. 10). Besides, the spark erosion method does not require crucible and the product has no contamination issues. Finally, oxygen-free preparation conditions are easily achieved.

1.4 Current Accomplishments in Bulk and Nanocomposite Thermoelectrics

Because of the interplay of the coefficients, and their strong dependence on temperature any TE material is limited to operate over the suitable temperature range. For the thermoelectric industry and applications, the classic inorganic and organic TEs are the most commonly used materials. So we will focus on the below discussion on the recent progress of the inorganic and organic TEs temperature range dependant.

1.4.1 Bismuth Telluride (Bi_2Te_3)

One of the most significant TE materials is Bi_2Te_3 based alloys & compounds which commonly used in the TE industry for enormous applications since1960. They have a rhombohedral crystal structure composed of five thick lamellae, (Te^1-Bi-Te^2-Bi-Te^1) where they are also called quintuple layers (QL). The QL layers pack along the c-axis via van der Waals interactions, whereas the Te^2 atoms are hybridized (sp^3d^2) to six Bi-atoms as illustrated in Fig. 11. At room temperature, the unit cell parameters take the values a = 4.345 Å and c = 30.483 Å. Moreover, the narrow semiconducting gap

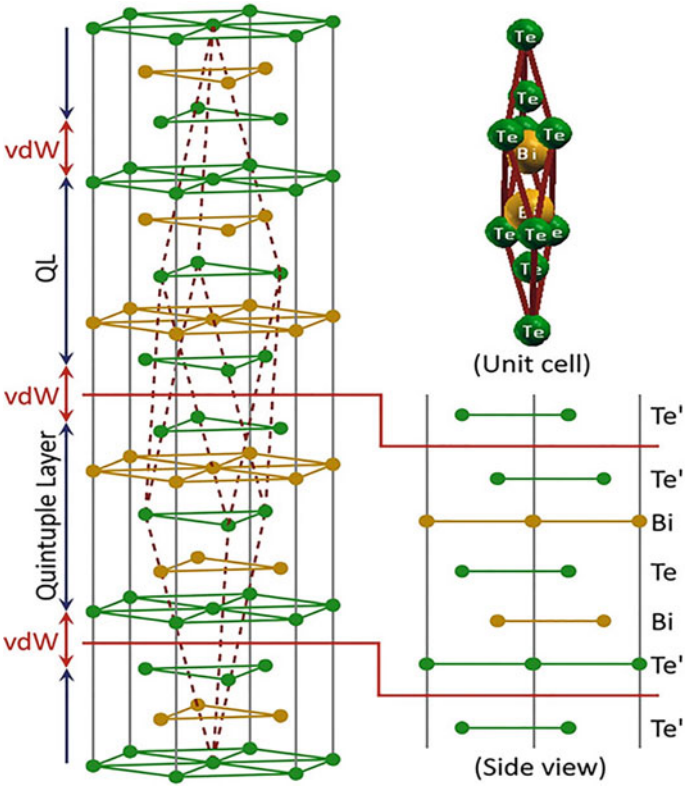

Fig. 11 Bi_2Te_3 Crystal structure showing van der Waals gaps (vdW) and the quintuple layers

at room temperature is equal to $E_g \sim 0.13$ eV makes these compounds beneficial for various TE applications. The excitations of the charge carriers are easier to excite into conduction band with increasing temperatures consequently, in the valence band an equivalent number of holes stay behind. These electron–hole pairs will play a part in the total heat conduction which may reduce the Seebeck coefficient (S). So, the usage of this material in high-temperature applications may enhance the energy gap also (Fig. 12).

The doping process results in a crucial outcome on Bi_2Te_3 starting from the type of the tuning and chaining the ZT values. The doping with Sb makes the Bi_2Te_3 alloys p-type semiconductor and the polycrystalline p-type $Bi_{0.5}Sb_{1.5}Te_3$ nanocomposites in bulk ($ZT = 1.2$ at 300 K & $ZT = 1.4$ at 373 K, respectively see Fig. 13). Also, the size reduction significantly condensed the thermal conductivity to 1.0 $Wm^{-1}\ K^{-1}$ in the nanomaterials from 1.3 $Wm^{-1}\ K^{-1}$ in the bulk ingots for the same materials, even though the electrical conductivity reduced slightly in the nano-composite. Finally, the achieved nanoscale materials enhance the ZT by 30% higher than that of bulk

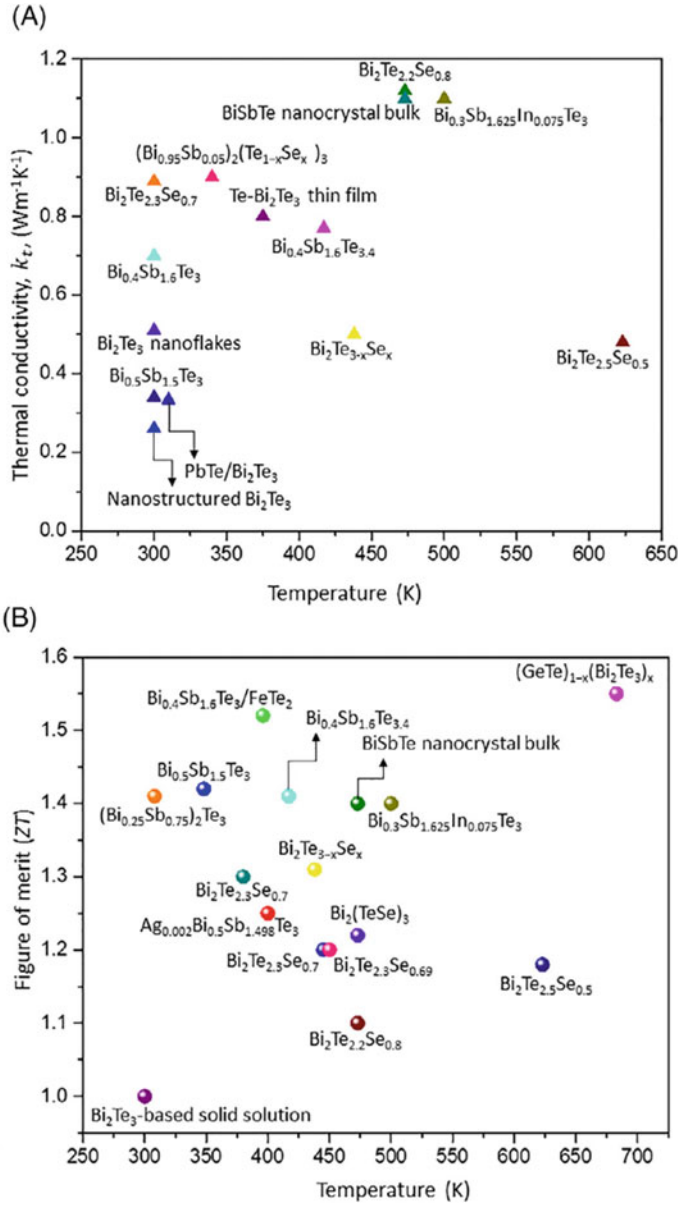

Fig. 12 Promising Bi_2Te_3 alloys displaying **a** ultra-low κ_T and **b** improved ZT values temperature dependence

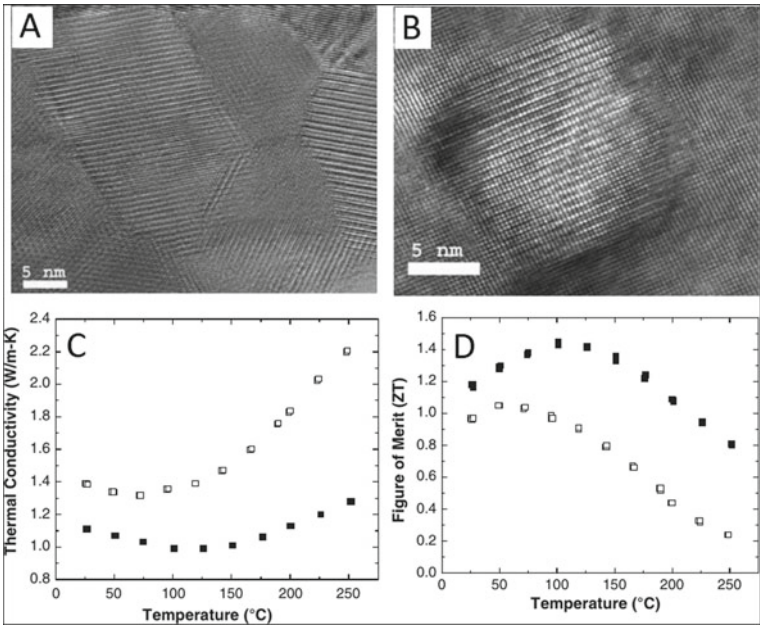

Fig. 13 High magnification TEM images of the hot-pressed $Bi_xSb_{2-x}Te_3$ nanostructured materials: **a** showing the nanosize, high crystallinity, random orientation, and clean grain boundaries. **b** Nanodots without grain boundaries. **c** Thermal conductivity and **d** ZT of the $Bi_xSb_{2-x}Te_3$ nanocomposites reproduced from Ref. Here white squares represent state-of-the-art p-type BiSbTe ingots and black squares display hot pressed bulk samples

ingots. To characterize the grain structure of the nanocomposite, Transmission electron microscopy (TEM) is illustrated in Fig. 8(a,c). From TEM data, it can be seen that the complex polygonal grain structures of few microns to a few nanometers size. At the same time, nanodots from Sb-rich ranged from 2 to 10 nm in diameter and a pure precipitate from Te with a diameter in the range 5–30 nm were also detected. The importance of these nanostructures could successfully scatter phonons with a wide wavelength, which improves the thermoelectric characteristics of the nanostructured Bi_2Te_3 composites. The more recent studies show other nanocomposites of p-type Bi_2Te_3-based compounds enhance the ZT to 1.3 and 1.4 at 75 K and 373 K, respectively, but the figure of merit displays a value of nearly 1.04 at 398 K in n-type Bi_2Te_3 nanocomposites.

Different studies on the characteristics of Bi_2Te_3-based nanocomposites display a wide variation in ZT values (0.4−1.7) at different temperatures. Such as a maxima in ZT equal to 1.5 at 390 $_K$ was obtained in p-type $(Bi,Sb)_2Te_3$ nanocomposites when single elements of Bi, Sb, and Te are melt-spun simultaneously and further pursued by the spark plasma sintering technique. Values like ZT(1.47) and ZT(1.56) were accomplished in nanostructures synthesized by the hot-pressing method of Sb_2Te_3

and Bi_2Te_3 powders at nanoscale range with diameters less than 20 nm and p-type $Bi_{0.52}Sb_{1.48}Te_3$ nanocomposite with the diameter ranging from 5–15 nm precipitates.

Also, *Sharma* and his group achieved the highest ZT value at 700 K equal to 2.42 for Bi_2Te_3 (p-type) samples, whereas Bi_2Te_3 alloys in n-type form show large κ_T due to small E_g as well as minority carriers (electrons). Various studies have been put forward to improve E_g and simultaneously decrease κ_T of n-type Bi_2Te_3 by the different methods such as doping, alloying, nanostructuring, nanocomposites, nanoplates, quantum dots and twin boundary engineering are the most common routes.

Furthermore, Shalaby et al. synthesized a sulfur-doped $Bi_2Te_{2.85}Se_{0.15}$ nano composites from n-type semiconductors with achieved E_g of 0.14 eV. On the other hand, Bi_2Te_3 n-type nanocomposites were fabricated with the help of (NaOH) and the obtained E_g was 4.8 eV which was much higher than that of the pure Bi_2Te_3 (0.13 eV). The defects and other impurities like the existence of dislocations at the grain boundaries play a curial and non-invasive role in κ_T reduction by scattering the minority carriers and preventing them from contributing to the electronic transport properties.

On the other hand, a liquid-phase compaction method was used by *Kim* and his group to enhance dislocation arrays at grain boundaries having low-energy (see Fig. 13). The major purpose of this approach is to scatter and diffuse the phonons with medium frequency so that the phonon thermal conductivity (κ_l) reduces. They also pronounced the κ_l reduction to 0.33 Wm^{-1} K^{-1} and an improvement of ZT = 1.86 at 320 K. Moreover, *Yang* and his co-workers fabricated n-type Bi_2Te_3 nanocomposites with ultra-low κ_l of around 0.2 Wm^{-1} K^{-1} by creating high-density grain boundaries through dislocations. Additionally, the composite of $Bi_{0.36}Sb_{1.64}Te_3$ loaded with reduced Graphene Oxide (RGO) displayed a small κ_l of 0.63 Wm^{-1} K^{-1}.

Hydrothermal/solvothermal technique has also been used to fabricate Bi_2Te_3 nanostructures. *Ni* and his coworkers prepared nanopowders of Bi_2Te_3 using this approach and the hot-pressed method with zone-melted Alloy has been used with a ratio of 10:90. They found that the reduction in the size of powders to nanoscale decreases the thermal conductivity robustly than the electrical conductivity, which results in the improvement of ZT (0.83). Moreover, the possibility of the achievement of ZT of the nanocomposites materialized because of the usage of the suitable dopants and the structural optimization of the base alloys. Other Bi_2Te_3-based nanocomposites demonstrate similar TE characteristics as that of pristine bulk Bi_2Te_3, whereas some in contrast displayed poor performances. In conclusion, TE operations are related strongly to the structural and compositional characteristics of nanocomposites.

1.4.2 PbTe Based Nanocomposites

Lead telluride (PbTe) being one of the promising TE materials works at medium temperatures ranging from (450–800 K). Recently, The ZT of these compounds was

almost doubled to 1.5 at 773 K for Th doped PbTe via the improvement of the Seebeck coefficient (S). High ZT Th-doped PbTe nanostructured materials were observed and the density of PbTe nanocomposites was 95% as that of theoretical predictions. Such samples were fabricated by spark plasma sintering technique with nanoparticles ranging from 100–150 nm. The figure of merit of these nanocomposites was around 0.1 at room temperature. Doping elements such as potassium were observed to affect the structural and thermoelectric properties of PbTe nanocomposites.

Experimentally at room temperature, when the Potassium content increases the electrical conductivity was slightly enhanced also but at higher temperatures no effects have been indicated, where all samples exhibited a reduction with temperature. Also, it was found that all samples have nearly the same thermal diffusivity. A slight change in Seebeck coefficients for all samples has probably remarked a consequence of hole contributions w.r.t high carrier concentration. Figure 14a illustrates that the PF was enhanced by the increase in potassium content and registered a peak at 500 K. The maximum ZT value for $K_{0.015}Pb_{0.985}Te$ reached 1.3 at 673 K (Fig. 14b), in comparison to that of the Sodium-doped PbTe at the same temperature.

The ball-milling technique followed by a hot-pressed process was used in Al_xPbTe nanocomposites fabrication as depicted in Fig. 15a. In addition, the Aluminum doped PbTe nanocomposites show n-type semiconductor behavior with Seebeck parameter in the range –100 to –200 V/K and the electrical conductivity values of 3.6–18 $\times$ 10^4 S/m at 300 K, and the highest ZT of 1.2 is achieved for the $Al_{0.03}PbTe$ nanocomposites at 770 K. SEM image of a cracked surface of Al-doped PbTe nanocomposite is shown in Fig. 10b. The temperature dependence of the thermoelectric properties at different doping levels of Cr in Cr-doped PbTe nanocomposites is depicted in Fig. 15. It was found that Cr doping increased the power factor dramatically around the room temperature in contrast to the other n-type PbTe alloys. Also, the thermal conductivity reduces to 1.3 W/m/K (at 773 K) from 2.6 W/m/K at 300 K.

Figure 16 illustrates the thermoelectric properties at various temperatures for $Cr_{0.01}Pb_{0.99}Te_{1-x}Se_x$ (x = 0.25, 0.5, 0.75, 0.85) systems. It was found that the nanocomposites make a reduction in electrical conductivity values with the increasing

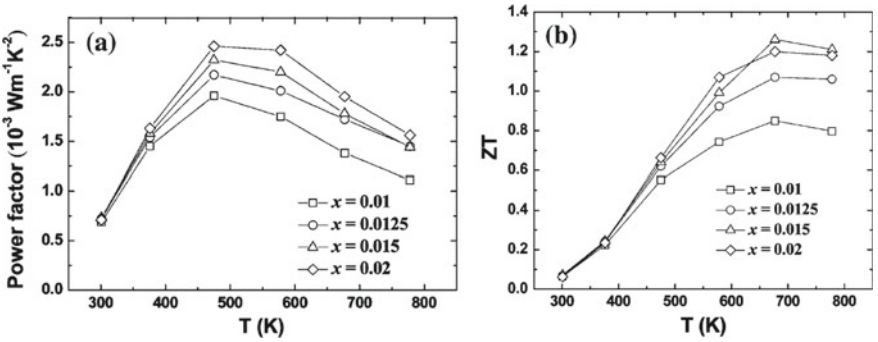

Fig. 14 The temperature dependence of: **a** power factor (PF) and **b** ZT of $K_xPb_{1-x}Te$ nanocomposite (x = 0.01, 0.0125, 0.015, 0.02)

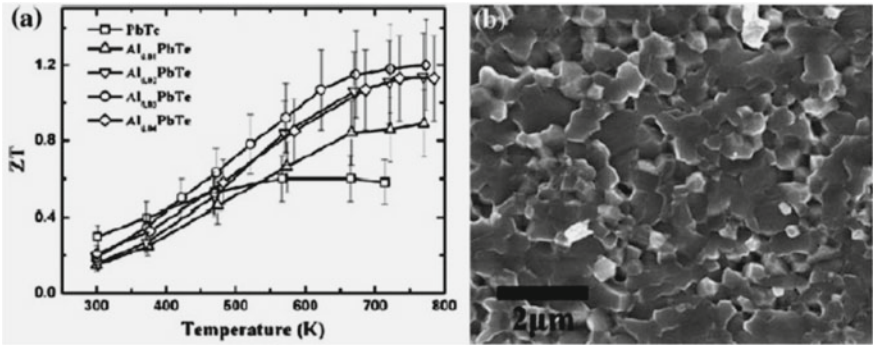

Fig. 15 The taken data for Al_xPbTe samples (x = 0, 0.01, 0.02, 0.03, 0.04). **a** Temperature versus ZT and **b** SEM images

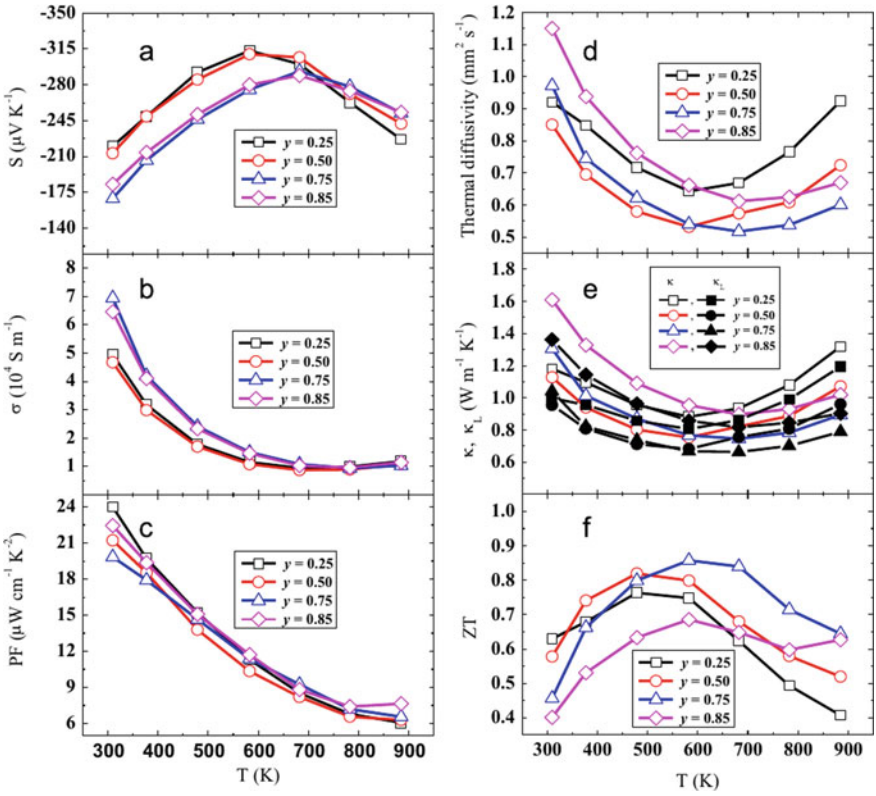

Fig. 16 Temperature-dependent thermoelectric parameters of $Cr_xPb_{1-x}Te$ nanocomposites (x = 0.01, 0.015, 0.025, 0.03) **a** Seebeck coefficient (S), **b** electrical conductivity, **c** power factor (PF), **d** thermal diffusivity, **e** total thermal conductivity (κ) and lattice thermal conductivity (κ_L), and **f** ZT

temperatures which is a characteristic of degenerate semiconductors. With enhancing Se content at a level of doping content into Cr site with 1 atomic %, the achieved Seebeck coefficient (S) reduced from 211 to 157 mV/K at room temperature. At higher temperatures, it was remarked that nanocomposites materials lower the Seebeck Coefficient because of the production of the bipolar effect. Generally, this effect shows a stronger behavior in samples with abundant Te concentration but it is still smaller in quantity than Se-rich samples. On the other hand, the increase of Se content to 75 atomic percent may enhance the electrical conductivity to the optimum because it drastically decreases when Se concentration was above 75 atomic %.

Se- rich- $Cr_{0.01}Pb_{0.99}Te_{0.25}Se_{0.75}$ sample revealed a high electrical conductivity and power factor throughout the temperature range. The enhancement was happened for the electrical conductivity due to the increase in the carrier concentrations to (8.12×10^{18} cm^{-3}) at room temperature proved from Hall measurements. This results show a remarkable drop in the thermal conductivity (κ), owing to the role of the defects resulting from alloying in phonon scattering, in comparison with the observed data from the Cr-doped PbTe nanocrystals.

At equal content of Te and Se in $Cr_{0.01}Pb_{0.99}Te_{0.5}Se_{0.5}$ nanomaterials, the thermal conductivity condensed to 0.8 W/m/K at 573 K. This was lower than 72% of the thermal conductivity achieved on PbTe for the same Cr doping level with 1% as depicted into Fig. 16. This decrease was expected theoretically and experimentally it was found to happen due to mass fluctuations when lattice distortion occurs. But the thermal conductivity at higher temperatures was registered and associated with the contribution of the heat transport from the minority carriers (holes). The highest figure of merit ZT for Se-rich $Cr_{0.01}Pb_{0.99}Te_{0.25}Se_{0.75}$ is 1 within the range of 573 K to 673 K. The maximum peak in ZT increased with increasing Se content.

It was found that Te-rich $Cr_{0.015}Pb_{0.985}Te_{0.75}Se_{0.25}$ nanocrystal has a maximum (ZT = 0.6) at room temperature due to the improvement of the thermoelectric performance by lowering κ, increasing (S = 220 mV/K) and the Hall mobility to 1120 $cm^2/V/s$ that improves the power factor. The figure of merit of Se-rich $Cr_{0.01}Pb_{0.99}Te_{0.25}Se_{0.75}$ samples was reported 0.5 at 573 and 1 at 673 K, respectively.

Besides, *Sie* and coworkers used Na_2Te as a doping material in PbTe alloy where a high S (-112 μVK^{-1}), σ (53.52 Scm^{-1}) and ZT of 0.81 were obtained. Also, *Jood* and his research group obtained a high ZT (~1.9) for the combinations (p-type $Pb_{0.953}Na_{0.040}Ge_{0.007}Te$) and (n-type $PbTe_{0.9964}I_{0.0036}$) legs by using between the dopants and the nanostructure of PbTe at ~805 K. Furthermore, *Xiao* et al. articulated the mix of Se with Sn and alloyed them into PbTe, where Se diminished the κ_T to ~1.21 from ~3 Wm^{-1} K^{-1} but Sn improved both the carrier concentration (n) and the mobility (μ) of PbTe. They achieved the ZT of 1.2 at 673 K as well as the PF of ~14.6 μWcm^{-1} K^{-1} at 300 K in their work. Consequently, the key point to enhance ZT to the highest values for PbTe alloys is striking to improve DOS to obtain a high thermoelectric power coefficient (S), and the reduction of κ_l value is also demanded with less effect on the electronic transport properties of these alloys.

1.4.3 Tin Selenide (SnSe) and Copper Selenide (Cu_2Se) Materials

Among the inorganic TE materials feasible in a medium temperature range with high performance and efficiency, SnSe based compounds are an asset. It reveals excellent features such as i) the long-range thermal stability, ii) simplistic nature or constitutes earth-abundant elements, iii) intrinsically ultralow lattice thermal conductivity κ_T, and iv) less toxicity. For crystal structure properties, SnSe takes NaCl structure and comprises a layered orthorhombic space group Pnma (Fig. 17a), and its unit cell dimensions are a = 11.501 Å, b = 4.153 Å, and c = 4.445 Å. On the other, it has a low indirect band gap of 0.86 eV with p-type conduction (i.e. hole concentration ~10^{17}–10^{18} cm^{-3}) and very high resistivity (ρ) (~10^{1}–10^{5} Ωcm) at 300 K. Consequently, one of the important issues is that the polycrystalline structure of SnSe material cannot be used for TE applications due to its very high room-temperature resistivity. The

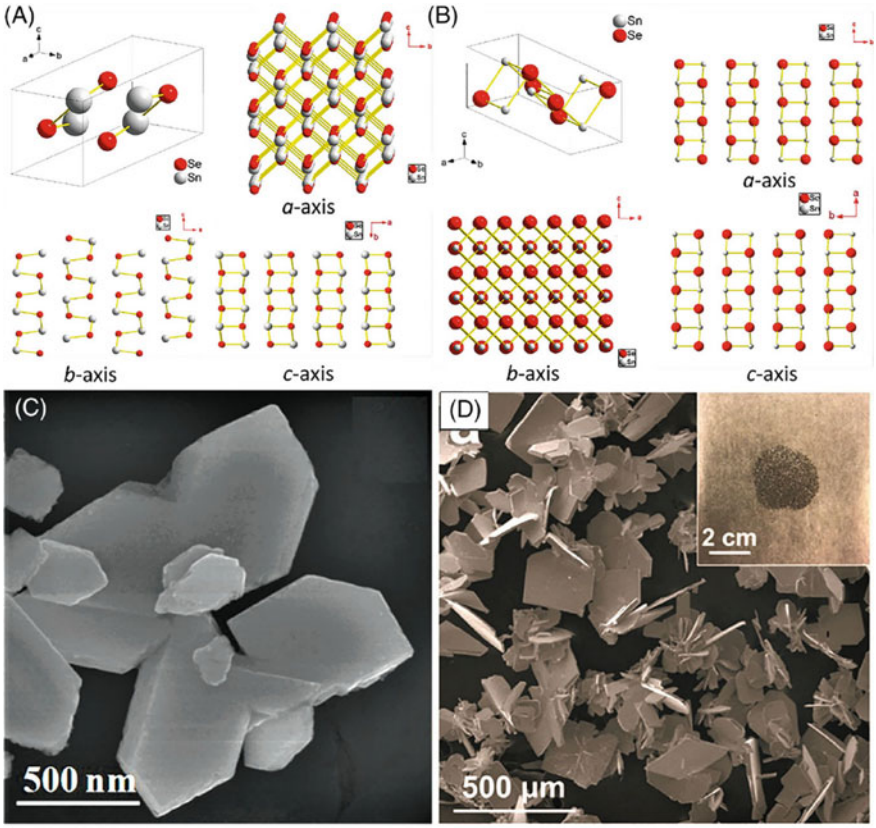

Fig. 17 SnSe Crystal structure with the common space groups **a** Pnma and **b** Cmcm, **c** Field Emission Scanning Electron Microscopy (FESEM) image of $Sn_{0.97}Ge_{0.03}Se$ nanoplates and **d** SEM and optical image (right top view) of prepared $Sn_{0.948}Cd_{0.023}Se$ microplates

increase in temperature ~750–800 K results in a remarkable phase change to Cmcm structure producing a further decrease in the energy gap to $E_g \sim 0.39$ eV and in lattice parameters to (a = 4.31 Å, b = 11.70 Å, and c = 4.31 Å) as shown in Fig. 16b. Polycrystalline SnSe usually displays low (μ) and thus shows low ZT value. The methods used to improve the performance of SnSe compounds are concluded to be suitable dopants as well as the low dimension scale or nanostructuring. For example, *Chandra* and his group used Ge doping elements to improve the n and diminish κ_T and their ($Sn_{0.97}Ge_{0.03}Se$ nanoplates) morphology is presented in Fig. 17c. They pronounced a very low κ_T (≈0.18 Wm^{-1} K^{-1}) and high ZT (≈2.1) at 873 K. Under similar conditions, *Shi* et al. revealed ~1.7 for ZT value of $Sn_{0.948}Cd_{0.023}Se$ micro-plates (Fig. 17d). In addition, *Liu* et al. employed simultaneous techniques of doping and nanostructuring to improve PF (5.43 μWcm^{-1} K^{-2}) and reduce κ_l (0.13 Wm^{-1} K^{-1}). SnSe nanocomposite was substituted by Pb and Zn atoms to form $Sn_{0.98}Pb_{0.01}Zn_{0.01}Se$ and maximum ZT (2.2) was recorded at 873 K. Due to the anisotropic transport characteristics of SnSe crystal system, mid-range TE performance was at its best. For example, a large ZT of 2.6 (at 923 K) and the ultralow thermal conductivities κ_T and κ_l with values ~0.35 and 0.23 Wm^{-1} K^{-1} at 973 K, respectively were obtained for the SnSe single crystals within the orthorhombic unit cell. At 800 K, *Chang* and his group attained an exceptional ZT value of 2 by improving the important two factors μ and S with the help of Br dopants in SnSe (a-axis). Although the very good TE properties were achieved from single phase SnSe systems such as the ultralow κ_T and outstanding ZT values there were some unwanted properties such as i) the poor mechanical properties, ii) the inflexible crystal growth nature, and iii) the high fabrication cost which in aggregate made it unfavorable for large-scale production.

From the first principle study, *Anish* et al. discussed the SnSe as p-type material with indirect band gap E_g of 0.66 eV, where a phase separation occurred and n-type character with negligible indirect band gap E_g of 0.064 eV was entertained. They also revealed the existence of $SnSe_2$ as a minority phase, whereas the possibility of Cu_2Se as a secondary phase is negligible because of its higher formation energy. Cu_2Se system is similar to SnSe with a potential application as TE materials due to its abundance and pollution-free nature. It has two crystal structures viz., α and β-phase. The Cu_2Se α-phase comprises a monoclinic structure with reasonably less symmetry at low temperatures. At 400 K, a remarkable structural change to a cubic system (β-phase within Fm-3 m space group) is observed, where Se atoms and Cu ions are redistributed on different interstitial sites and take up the simple face-centered cubic structure. The TE characteristics of Cu_2Se (β-phase) exhibits larger ZT value than that of α-phase because of the improvement of S, σ, PF, and decrease in κ_T. Even though the improvement of n raised σ decreases S and vice versa, which is not favorable for PF of TE materials. Metallic Cu_2Se β-phase reveals an outstanding PF (2.3 Wm^{-1} K^{-2}) as well as ultra-high ZT value at 400 K. The doping and the nanostructuring strategies are widely used to elevate the TE performance of Cu_2Se. *Liu* et al. for example used iodine (I) as a dopant to control the transition temperature of Cu_2Se system and thus large ZT value of 2.3 was achieved at 400 K. At the same time, *Hu* and his group used alkaline metal (Li) in the doping process to increase S where they articulated ZT of 2.14 for $Cu_{1.98}Li_{0.02}Se$ at 973 K. On the other hand,

Yang and his coworkers used a nanostructuring strategy to minimize the κ_l up to ~0.2 Wm^{-1} K^{-1}, which in turn shoots the ZT value to1.82 at 850 K. Carbon-based alloys used in Cu_2Se to enhance the thermoelectric power (S) and lower the κ_T for more efficient TE performances have been lately introduced. Such as, *Hu* et al. doped carbon nanodots into the Cu_2Se system that improved S to ~290 μVK^{-1} and diminished κ_T to 0.45 Wm^{-1} K^{-1} which resulted in ZT equal to 1.98 at 973 K. Also, *Li* and his group used nanoparticles of carbon-coated boron in Cu_2Se system which displayed ZT ~2.23 at 1000 K. Likewise, *Li* et al. engineered graphene nanoplates inside a Cu_2Se matrix which drastically reduced κ_T to ~0.4 Wm^{-1} K^{-1} and hence the ZT ~2.44 at 873 K was obtained. All these considerable improvements indicate the benefits of both SnSe and Cu_2Se systems as strong candidates for TE applications.

1.4.4 Skutterudites Nanocomposites

Skutterudites being extensively studied for potential thermoelectric processing are considered as promising choices for next-generation TE materials and applications especially for power generation used in both solar source and waste heat managements. The significant characteristic of this kind of TE material is the open cage-like structure where the filled atoms act as rattlers for phonons. The "rattling" of these doped atoms scatter the phonons effectively and significantly decreases the thermal conductivity (κ).

Generally, the common chemical formula of Skutterudites was established by Oftedal and take (MX_3) formula, where (M) is a transition element (Co, Rh, Ir…) and (X) imply Pnictogen (P/As/Sb) atoms. Binary Skutterudites consists of an open casing structure with an Im3 space group in a cubic body-centered unit cell structure, whereas the void is produced by eight atoms surrounding octahedrally as depicted in Fig. 17a. Moreover, the unit cell is repositioned by (1/4) distance diagonally across the body. On the other hand, the structure of Skutterudite composites contains two filled voids in each unit cell where the filler atoms are electropositive for example Yb, In, and Ti. An icosahedral cage-like structure surrounds these filler atoms taking the shape of pnicogen octahedral atoms (X). Moreover, the transition metal atoms (T) like Co, Rh, Ir, Ni, Pd are centered in this structure which takes the form of $EP_yT_4X_{12}$, depicted in Fig. 17b. This is called a "filled Skutterudite" and was first experimentally synthesized in 1977 by Jeitschko et al. (Fig. 18).

It is well known that most of the binary skutterudite TE materials exhibit high μ and n as mentioned in ref. [260]. For example, the $CoSb_3$ compound achieved a very high μ and n of 3445 $cm2V^{-1}$ s^{-1} and 4×10^{17} cm^{-3}, respectively. On the other hand, the undoped p-type $CoSb_3$ exhibits a ZT value of about 0.2, and the doping in n-type crystals attains ZT = 0.52 at 600 K. The achieved figure of merit value in $(Ni, Co)_4Sb_{12}$ nanocomposites is 0.7 without rattlers. Also, *Khovaylo* and his group achieved an ultra-low κ_T close to 1.25 and a high ZT value of ~1.5 at 725 K with the help of indium filler atoms embedded in skutterudite Co_4Sb_{12} composition. Typically, the improvements in ZT were obtained with various kinds of atoms (such as Ce, La, Ca, Ba, Yb) to fill the cages structures. For instance, Yb-filled n-type $Yb_{0.19}Co_4Sb_{12}$

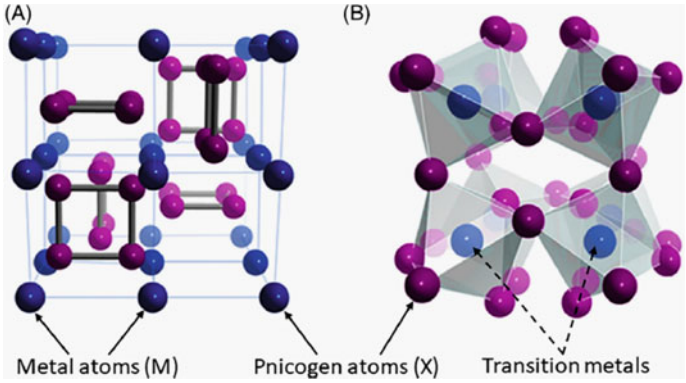

Fig. 18 The representative figures of **a** Binary Skutterudites structure with metal atoms (M), pnictogen atoms (X), and **b** general structure of filled ($EP_yT_4X_{12}$) Skutterudite

composition recorded a ZT peak close to 1 at 373 °C and ZT was about 0.7 value at 400 °C for n-type $Yb_{0.15}Co_4Sb_{12}$. While using the ball-milling and hot-pressing approach, the peak of ZT for $Yb_xCo_4Sb_{12}$ nanocomposites increased to 1.2. More categories of doped Co_4Sb_{12} nanocrystals have been articulated, like $Sn_yFe_3Co_5Sb_{24}$, $FeCo_3Sb_{12}$ as well as the rare-earth filled Fe_4Sb_{12} Skutterudite nanocomposites. *Zhou* and his group studied the p-type skutterudite nanocomposites $Co_{0.9}Fe_{0.1}Sb_3$ with $FeSb_2$ nano-inclusions. Generally, $FeSb_2$ is a chemically stable compound found as a secondary phase p-type skutterudite. For instance, the nanocomposite samples of $Co_{0.9}Fe_{0.1+x}Sb_{3+2\times}$ with $x = 0.05$, 0.1, and 0.02.

The lower Sb content is very sensitive in the constriction of $FeSb_2$ so rapid solidification was used to facilitate this process in the skutterudite stoichiometry. FESEM images on the fractured surface of the bulk $Co_{0.9}Fe_{0.1+x}Sb_{3+2\times}$ nanocomposites are depicted in Fig. 19. Figure (19a) illustrates the zoomed-in examination of the circle region where nano-sized particles can be seen. It appears that the nanoparticles can be found in Fig. 19 (a−c) with different nominal (x) content where Fig. 19 (d) represents the parent sample $Co_{0.75}Fe_{0.25}Sb_3$ which is having the same Fe/Co ratio as $x = 0.2$ content and has the normal skutterudite composition MX_3. It has appeared from Fig. 19d that the grain boundaries are much cleaner due to the Fe substations and shared in $FeSb_2$ skutterudites nanoparticles and it was found to be grown to the micron size. Even though the Skutterudites reveal high κ_T, but most of the Skutterudites give high $ZT \geq 1$ so it offers a strong potential for using them in high-efficiency TE applications.

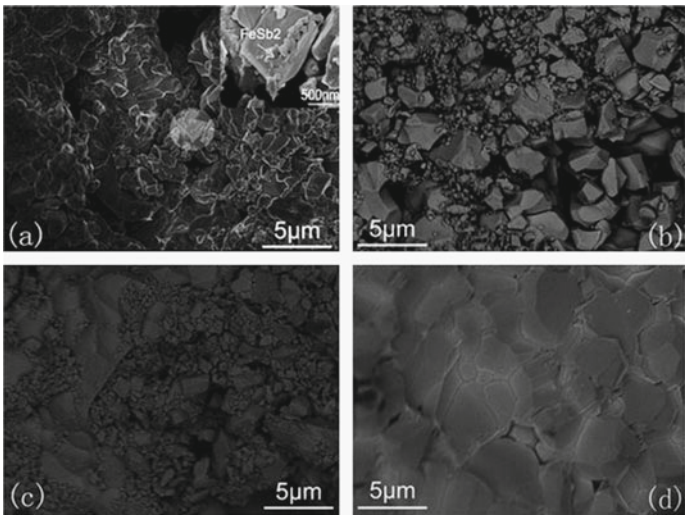

Fig. 19 FESEM images on fractured surface of $Co_{0.9}Fe_{0.1}Sb_{3+x}FeSb_2$ nanocomposites and reference sample $Co_{0.75}Fe_{0.25}Sb_3$. **a** x = 0.05, the circular region represents the nano-sized particles; **b** x = 0.1; **c** x = 0.2; **d** $Co_{0.75}Fe_{0.25}Sb_3$

1.4.5 Mg_2Si-Based Nanocomposites

Mg_2Si-Based Nanomaterials are considered as TE materials due to the exhibition of high ZT, abundant, non-toxic, and light elemental compositions e.g. Mg_2(Si, Sn), and become more attractive. A large ZT value of ~1.1 was achieved at 800 K for doped Mg_2(Si, Sn) typically in $MgSi_{0.4}Sn_{0.6}$ solid solutions, which is analogous to PbTe and filled skutterudite type materials. *Zhang* and his co-workers carried out the full microstructure study and thermoelectric properties of high ZT $Mg_2Si_{0.4-x}Sn_{0.6}Sb_x$ alloys. The obtained value of the lattice thermal conductivity κ_l was in the range 1.5–2.1 W/mK at 300 K which is quite small when compared to undoped-Mg_2Si (7.9 W/mK) and 5.9 W/mK of Mg_2Sn composites. One of the important remarks on the synthesis procedure is the observation of the in situ formed nanodots by phase separation approach. So, it is proposed that the formations of the nanoscale compositional or the structural modulations are the reasons behind the reduction of thermal conductivity in these samples.

On other hand, Mg_2Si/Si nanocomposites were prepared by *Yalei Huang* and his group and the compositions comprise Si nanosheet bundles. Also, the Mg_2Si deposited and formed on the Si nano-sheet bundles was prepared by the thermal annealing of $CaSi_2$ powders in $MgCl_2$ vapor. Figure 20 (a,b) illustrates the morphology obtained from SEM and TEM images of the Mg_2Si/Si composites synthesized on the Si (111) substrate. The nanosheets were obtained with a thickness of several tens and up to one hundred nanometers and the stacked nanosheets also appeared with a small void space to form the bundles. Figure 20 (c,d) displays the

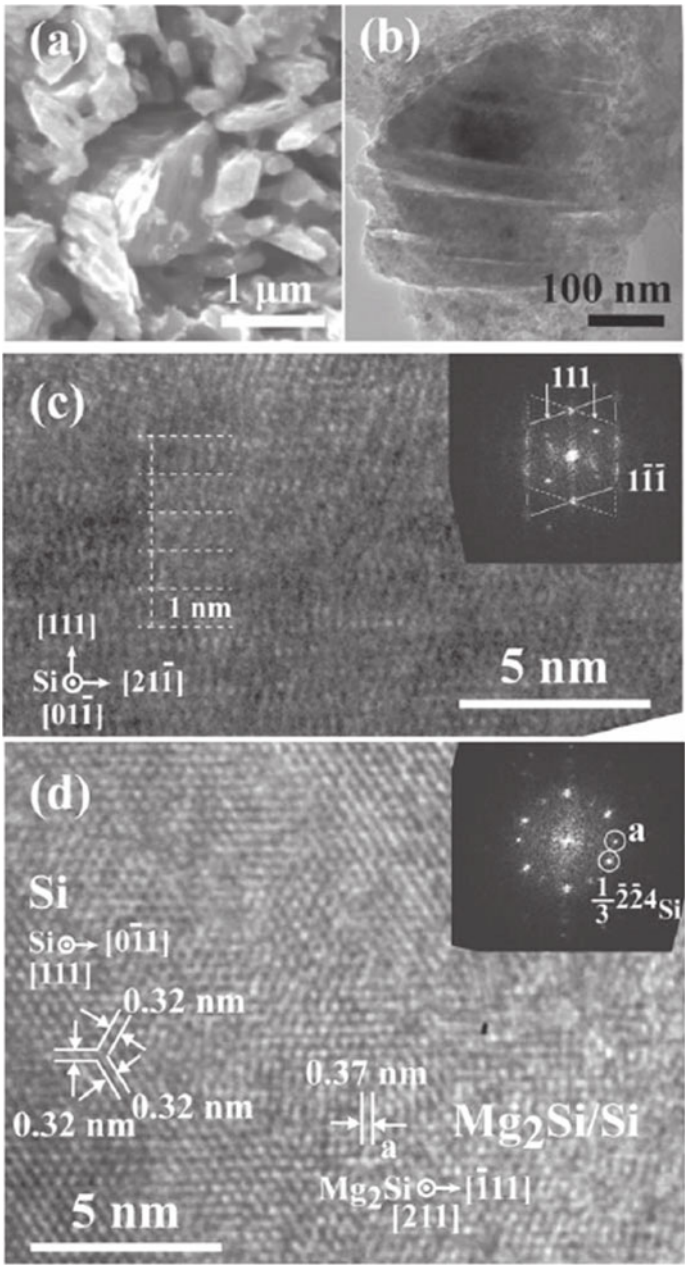

Fig. 20 A schematic diagrams for **a** Plan-view SEM image, **b** TEM image, **c** cross-sectional and **d** Plan view HRTEM images with an FFT pattern of the nano-sheet synthesized from $CaSi_2$ micro-walls on a Si (111) substrate by the thermal treatment approach at 600 °C

cross-sectional and plan-view for HRTEM images with FFT patterns of the synthesized composites scratched off the substrate. Recently, *Souda* et al. carried out the modulation doping in Si–Mg_2Si system, where Mg_2Si was considered heavily doped phase and Si the undoped phase. Also, the Si–Mg_2Si nanocomposite ribbons were obtained by a melt spinning technique. The thermoelectric properties of the prepared samples are determined with a large power factor value equal to 2.7 mW m^{-1} K^{-2} at 773 K for these ribbons within the optimized structure and chemical compositions.

1.4.6 Si-Ge Nanocomposites

Alloys and nanocomposites of Si and Ge describe the solid solution Si_xGe_{1-x} thermoelectric materials operating at temperatures more than 1000 K. For instance, SiGe based alloys are being used in radio-isotope TE generators (RTG) for various space missions because of their ability to convert radio-isotope heat into electricity at large temperatures [52]. Generally, SiGe alloys possess potential applications in thermoelectric generators (TEG) to regain waste heat. Si and Ge in Si-Ge alloys crystallize in the diamond-like structure with the Fd-3 m space group which takes the face-centered cubic (FCC) Bravais lattice. SiGe composites have two well-known characteristics; viz the melting point is very high ~1300 K and outstanding stability at high temperatures. Also, Si_xGe_{1-x} solid solutions have good chemical stability at high temperatures, specifically against the oxidation process. A high figure of merit (<~1) entitles the fundamentals of TE use at a high-temperature range (1000–1200 K). Owing to their rigid and symmetric crystal structure, they display extremely small room temperature thermal conductivity (κ) (150 and 63 W/mK, respectively) to become promising thermoelectric materials. Nevertheless, the thermal conductivity has been decreased to nearly 5–10 W/mK due to the formation of a solid solution alloying. Recently, a lot of theoretical and experimental groups put forward massive efforts and achieved some success in improving the ZT of Si-Ge alloys. Nanostructuring using ball milling and other techniques is one of these efforts by which the thermal conductivity is reduced in comparison to the bulk alloys. The peak of ZT for both p-type and n-type Si-Ge alloys has been achieved [44, 45]. Particularly the figure of merit ZT of n-type Si-Ge nanocomposite has gone beyond 1 (at 1100 K). Figure 21 exhibits the power factor (PF) as well as the thermal conductivity (κ) of the $Si_{80}Ge_{20}$ systems synthesized by ball milling and hot-pressing approach. On the other hand, the Nanostructuring impact appears when the interfacial phonon scattering and the low dimensionality (nanoscale size) make the SiGe superlattices nanowires furnish a low κ_T. For example, *Usenko* and his research group synthesized the bulk sample of n-type Si-Ge nanostructures employing ball-milling and spark plasma sintering techniques. The obtained sample showed a little κ_T of about 2.47 Wm^{-1} K^{-1} at 300 K and an enhanced ZT value of 1.1 at 1073 K.

Various studies showed that the figure of merit (ZT) for n-type Si-Ge alloys (1 at 900–950 °C) is higher than p-type SiGe (0.65 at 900 °C) due to the large κ_T value and maximum n. In some cases, the ZT obtained for n-type Si-Ge alloy was about 1.3 with κ_T equal to 2.8 Wm^{-1} K^{-1} recorded at 1173 K, whereas p-type Si-Ge has reached a

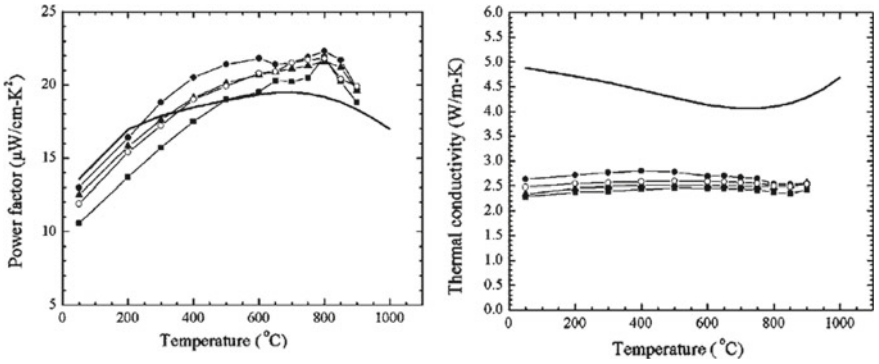

Fig. 21 Schematic diagrams for p-type $Si_{80}Ge_{20}$ nanocomposites: on the left) the power factor results, and on the right) thermal conductivity results of the samples prepared with the assistance of ball milling, hot pressing, and annealing approach

ZT value ~0.5. Another effort has been endeavored to minimize κ_T and boost the ZT of Si-Ge alloys via doping. Typically, dopants have achieved a reasonable ZT value and lowered the κ_T values as well. *Usenko* et al. used boron as a dopant in $Si_{80}Ge_{20}$ via the spark plasma approach. They obtained a low κ_T value (~2.9 Wm^{-1} K^{-1}) for the prepared samples and achieved a high ZT value of 0.72 at 1073 K. Later, *Peng* et al. exhibited a boron-doped Si-Ge thin film. They articulated an enhancement in S to 850 μVK^{-1} at 473 K but lowered the ρ to 1.3 $\times$ 10^{-5} Ωm where the PF improved to 5.6 $\times$ 10^{-2} Wm^{-1} K^{-2}. Also, the high-energy ball milling technique was used to obtain single-phase p-type (boron-doped) $Si_{80}Ge_{20}$ nanoparticles from elements [45]. (Fig. 22a) illustrates the single-phase synthesized $Si_{80}Ge_{20}B_x$ alloys. The crystalline nature of the mechanically alloyed Si-Ge nanocrystals differs from that of the ball-milled Bi_2Te_3 nanocrystals where Fig. 22(d) showed the polycrystalline nature of $Si_{80}Ge_{20}B_x$ nanoparticles. It appears that the mechanically alloyed Si-Ge is consisting of several sub-nanograins as depicted in (Fig. 22d). HRTEM image in Fig. 22(d) reveals the existence of a lot of defects inside the individual sub-grain since the formation of the nanograins was developed by a low temperature mechanical alloying technique rather than the melting and solidification method at higher temperatures.

Alternatively, the obtained n-type $Si_{80}Ge_{20}P_2$ samples prepared via mechanical alloy technique gave a single-phase nanoparticle shown in Fig. 23 (a). The particle size of the as-prepared nanopowders was ranging from 30–200 nm as depicted in Fig. 23 (b,c). These nanoparticles are like p-type mechanically alloyed Si-Ge nanoparticles where sun-grains from small crystals were visualized. The obtained sub-nanograins range from 5–15 nm as depicted in Fig. 23 (d). The main goal for thermoelectrics is to reduce κ_l. So one of the interesting perspectives of Si-Ge alloy is the reduction of (κ_l) via different composites and preparation methods. For instance, *Kikuchi* and his coworkers used 10 nm diameter SiNWs to be embedded into $SiGe_{0.3}$. Bio-template masking and neutral beam etching methods were used to achieve SiNWs and then deposited via chemical vapor deposition route thermally.

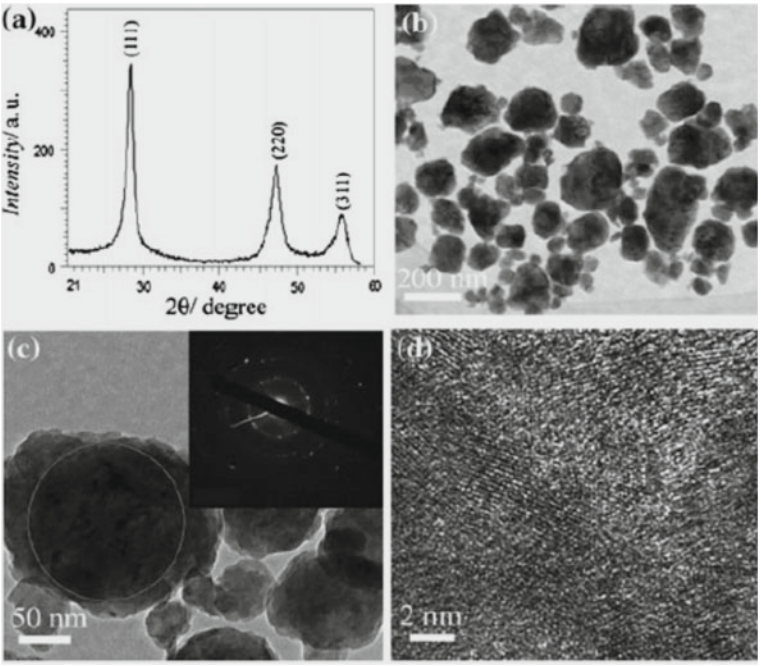

Fig. 22 Schematic diagrams for p-type $Si_{80}Ge_{20}B_x$ nanoparticles: **a** XRD pattern, **b** BF-TEM image, **c** medium magnification TEM image, **d** HRTEM image. The inset on the right of **c** is SAED of an individual grain revealing the polycrystalline structure of the grain [45]

They obtained from SiNW-$SiGe_{0.3}$ composite film a thickness of 100 nm, κ_T value of 3.5 ± 0.3 Wm^{-1} K^{-1} in the temperature range 300 to 350 K. Furthermore, they observed the S and σ values at 873 K to be 4.8×103 μVK^{-1} and 4.4×10^3 Sm^{-1}, respectively. *Usenko* et al. fabricated the n-type $Si_{0.9}Ge_{0.1}$-Mg_2Si composites. At 1073 K, they achieved a reduction in κ_l up to 1.4 Wm^{-1} K^{-1} and observed an average value for ZT of ~0.8.

1.4.7 Zintl Phases

The Zintl phases named after their discovery by a German chemist called Eduard Zintl and then were identified by Laves in the early 40s of the last century. A unified class of electropositive cations, mostly group I or II elements, reflect the Zintl phases. The second partner, which is a subset of inter-metallic compounds, was composed of post-transition metals or metal alloys from XIII, XIV, XV, XVI. Even though the application of Zintl phases as outstanding thermoelectrics is quite evident, their structure and chemical bonding details were fully investigated recently. Zintl phases may be widely used as TE materials due to the exhibition of the high thermoelectric

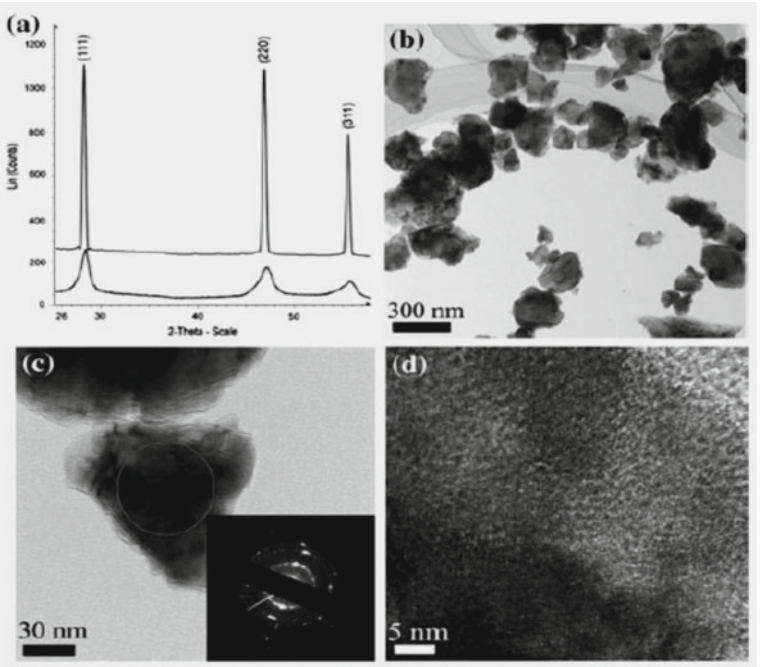

Fig. 23 Schematic diagrams of n-type $Bi_{80}Ge_{20}P_2$ nanoparticles as follow: **a** XRD diffractogram, **b** BF-TEM image, **c** BF-TEM image at medium magnification, and **d** HRTEM image. The inset on the right of **c** represents a SAED diagram of an individual nanoparticle [44]

power (S). For example, $Yb_{2-x}Eu_xCdSb_2$, $Mg_3Pb_{0.2}Sb_{1.8}$ and $Yb_{14}MgSb_{11}$ compositions registered the highest S values as follows 269 μVK^{-1}, ~280 μVK^{-1} and 279 μVK^{-1}, respectively.

Additionally, the best advantage of these materials is the flexibility to work in wide temperature ranges. p-type and n-type of Zintl(1-2-2) phases exhibit outstanding characteristics among Zintl compounds in the low till the middle-temperature ranges wherein the range 975−1275 K demonstrates an improvement in the other p-type Zintl(14-1-1) families. One of the promising Zintl phases is of kind $A_{14}MPn_{11}$, where (A) element labels alkaline-earth or rare-earth metal, (M) element describes transition or main group metal, and (Pn) defines a pnictogen, respectively. For instance, $Yb_{14}MnSb_{11}$ is the most superior TE material for high-temperature applications. Al, Zn and La- $Yb_{14}MnSb_{11}$ have attained a ZT = 1.1 at 1275 K, 1.3 at 1223 K and 1.15 at 1150 K, respectively. Moreover, *Snyder* et al. articulated that $Yb_{14}Mn_{0.67}Zn_{0.33}Sb_{11}$ and $Yb_{14}Mn_{0.8}Al_{0.2}Sb_{11}$ compounds show the highest ZT among the other doped $Yb_{14}MnSb_{11}$ phases at 1200 K with values 1.7 and 1.76, respectively. Furthermore, there are numerous Zintl compounds like: n-type of KSnSb (with ZT = 2.2 at 800 K and 0.6 at 300 K), $Ca_{0.5Yb0.5}Mg_2Bi_2$ (Zt = 1 at 873 K), $Mg_{2.985}Ag_{0.015}Sb_2$ records 0.15 at 725 K, $EuZn_2Sb_2$ and Yb- doped $EuZn_2Sb_2$ have ZT equal to 0.9 at 713 K and 0.68 at 773 K, ZnInSb compounds provide high ZT values of 1.4 at 700 K and

are commonly used for high-temperature applications. Lately, Mg_3Sb_2 based Zintl compositions with ZT value 0.6 at 773 K are very desirable for TE applications due to less toxicity, environment-friendly and earth-abundance characteristics.

More research has been carried out to study the possibility of transformation of p-type into n-type Mg_3Sb_2 compounds by terminating Mg vacancies and enhancing the number of carriers (n) to improve the TE performance of Mg_3Sb_2. *Li* and his coworkers theoretically studied the electronic structure of n-type Mg_3Sb_2 via density functional theory (DFT) and reached a very high value of ZT with 3.1 at 725 K. Later in another example within the same DFT constraints, they touched a ZT value of 2.75 [305]. However, no experimental works or results have yet been achieved to reproduce the ZT value of more than 2 in such compounds. Figure 24 shows the (HRTEM) images and EDX obtained data of the nanostructured Mg_3S_{b2} and $Mg_3Sb_{1.8}Bi_{0.2}$ alloys [306] which generally exhibits the nanoscale characteristics and represents the uniform microstructures with nanoscale crystallites, together with some microstructure defects (Fig. 24 b−e) resulting from the long hours of the ball-milling procedure [306].

Bhardwaj et al. demonstrated that the nanostructured Mg_3Sb_2 and $Mg_3Sb_{1.8}Bi_{0.2}$ prepared via high energy ball milling and then followed by spark plasma sintering approach yield a ZT of ~0.4 and ~0.94 at 773 K, respectively. These are 54% to 56%, higher than that of bulk specimens. The observed ZT values for the $Mg_3Sb_{1.8}Bi_{0.2}$ nanocrystals w.r.t temperature are depicted in Fig. 25.

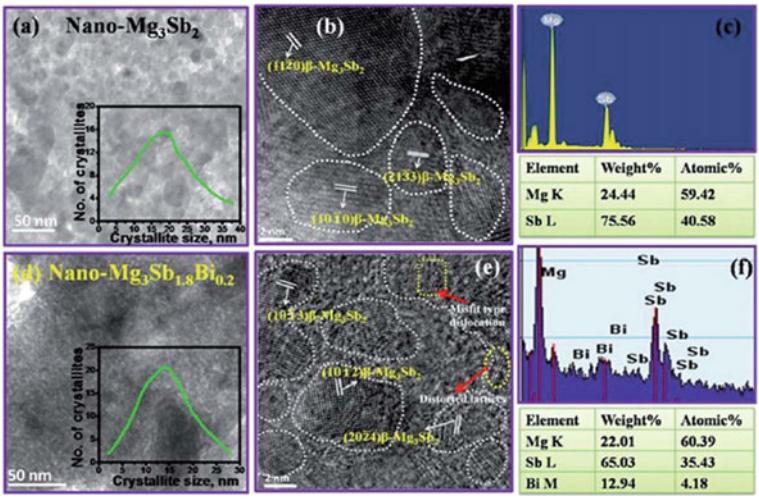

Fig. 24 Schematic diagrams nanostructured Mg_3S_{b2} and $Mg_3Sb_{1.8}Bi_{0.2}$ alloys: **a** TEM image of Mg_3Sb_2 sample; **b** nanostructured Mg_3Sb_2 lattice scale image with several orientations of the crystallographic planes; **c** EDAX-TEM designs for nanostructured Mg_3Sb_2 sample; **d** Obtaining data of bright field electron micrograph nanostructured $Mg_3Sb_{1.8}Bi_{0.2}$ sample; **e** The HRTEM of nanostructured $Mg_3Sb_{1.8}Bi_{0.2}$, showing distorted lattices; **f** The EDAX-TEM patterns obtained from the nanostructured $Mg_3Sb_{1.8}Bi_{0.2}$ specimen with the exact elemental analysis

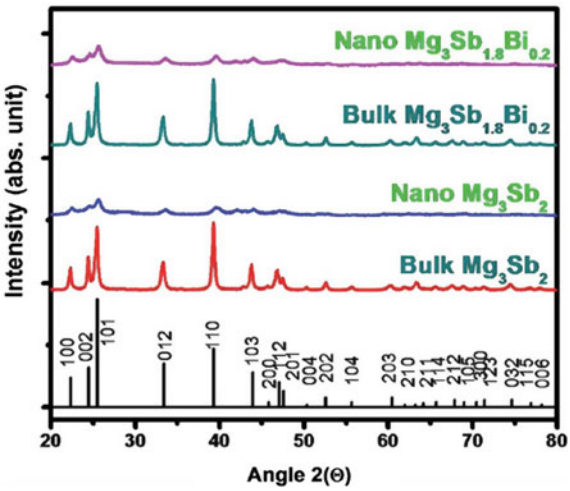

Fig. 25 The obtained data for the temperature dependence of the thermoelectric figure of merit of bulk $Mg_3Sb_{2-x}Bi_x$ (x = 0 & 0.2) samples

1.4.8 Heusler Materials

Heusler Alloys have long been discovered by F. Heusler in 1903. These alloys are broadly distributed in three categories according to the number of atoms in their unit cells. First, the Half-Heusler alloys having XYZ formula and are found in F-43 m space group. Here, the lattice positions are: X(0,0,0), Y(0.5,0.5,0.5) and Z(0.25,0.25,0.25). Second are the X_2YZ type Full Heusler alloys with L_21 structure (space group: Fm-3 m) and the atomic coordinates are X(0.75,0.75,0.75) and (0.25,0.25,0.25); Y(0,0,0) and Z(0.5,0.5,0.5). This class can be found in another stereotype called the inverse Heusler alloys with space group F-43 m but the position of X and Y atoms vary as: X(0,0,0) and (0.75,0.75,0.75), Y (0.5,0.5,0.5) and Z (0.25,0.25,0.25) depicted in Fig. 26. And the third one is the recent most category known as Quaternary Heusler Alloys with XX′YZ formula and these can be found in F-43 m structure within type-I, type-II and type-III; where X, X′, Y and Z locations vary as given in Fig. 25. Here, the X, X′, Y are mainly transition metal elements but can be a rare-earth also and Z atom is generally a p-block element.

However, these materials lately flourished in various technological applications due to the exhibition of magnificent properties ranging from half-metallic ferromagnetism to superconductivity, large Curie temperature, semiconductor or topological behavior, robust spin polarization, and shape memory effects, etc., They found applications in tunneling magnetoresistance (TMR) devices, spin injectors or magnetic tunnel junctions and magnetic read heads. At the same time, the potential application in thermoelectric power generation has been the eminent among all such properties. In view of the electronic structure, this huge class of materials consist of magnetic, nonmagnetic, semiconductors, half-metals, semimetals (spin-gapless semiconductors, Dirac or Weyl semimetals, spin semimetals), etc. Non-magnetism and semiconducting properties in Heusler alloys are preferably defined by Slater-Pauling rule

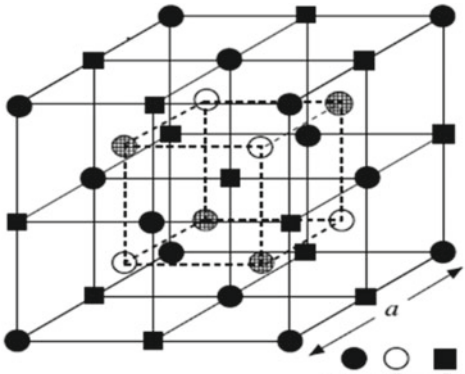

	A	B	C	D
Semi–Heuslers ($C1_b$) : XYZ	X	Y		Z
Full–Heuslers ($L2_1$) : X_2YZ	X	Y	X	Z
Quaternary Heuslers : (XX')YZ	X	Y	X'	Z
Inverse Heuslers (XA) : X_2YZ	X	X	Y	Z

Fig. 26 Schematic representation of the half- and full-Heusler compounds' various structures. Note also that the lattice would simply be the b.c.c. if all atoms were identical

(M = Nv-24 or 28 or 18); where the valence electron count (N_v) is linked to the total magnetic moment (M) of the crystal. The rigorous degenerate valence bands and fully compensated spins in 12 or 8 bands create the possible semiconducting electronic structure of these alloys. However, in some cases, the crystal symmetry or d-electron splitting leads to spin semi-metallic or spin gapless nature also.

Thermoelectric resourcefulness of Heusler materials have been precedented by the recent discovery of ZT = 5 or 6 in a metastable $Fe_2V_{0.8}W_{0.2}Al$ Heusler thin film are illustrated into Fig. 27. It was supposed that the large differential density of states and a Weyl-like dispersion of electrons present around the Fermi level initiates a high mobility of charge carriers [316]. Experimentally found Ti/Sn doped NbFeSb [317] and TaFeSb [318] Heuslers achieved a ZT equal to 1.1 and 0.5, respectively. Also, the p-type alloys including Fe(V,Nb)Sb [319], TiPdSn [320] and XCoSb (X = Ti, Zr, Hf) and n-type XNiSn with quite high ZTs are among the few to note down here.

However, different strategic criteria and alterations are meticulously put forward to shape the maximum efficient Heusler materials to exhibit the augmentation of electricity from waste heat. Since then a huge database of Heusler thermoelectrics has been scrutinized and maintained but more research is yet needed to improve the efficiency of these new materials.

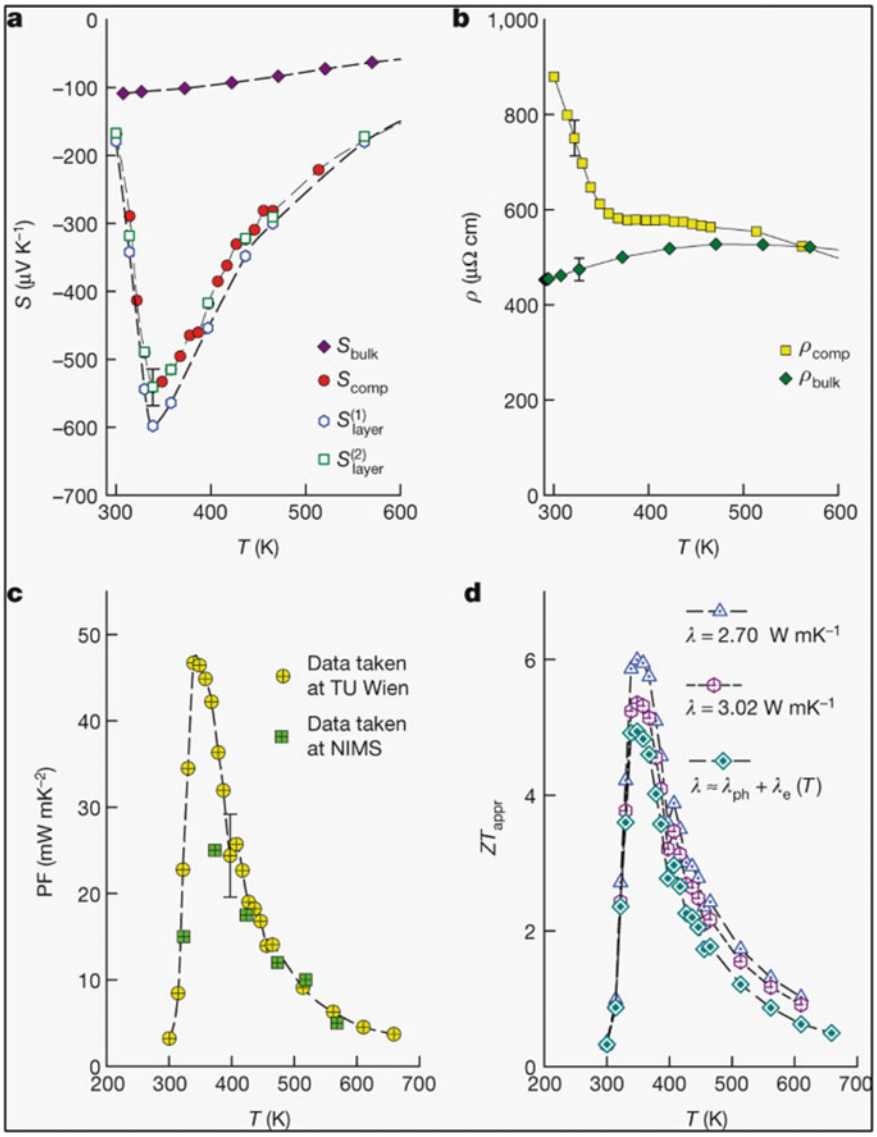

Fig. 27 Thin-film $Fe_2V_{0.8}W_{0.2}Al$ and its temperature-dependent thermoelectric properties. **a**, **b**, the Seebeck coefficient **a** and the electrical resistivity **b** of the entire composite (layer, interface and substrate), along with the $Fe_2V_{0.8}W_{0.2Al}$ thin-film. $S^{(1)}{}_{layer}$ and $S^{(2)}{}_{layer}$ are the Seebeck data with and without Fe_2Si as the interface, respectively. **c**, **d**, The power factor versus temperature **c** and the average merit figure **d**. ZT_{appr} is evaluated to a first approximation using the room-temperature (25 °C) thermal conductivity ($\lambda^{diff}{}_{RT} = 2.70\ Wm^{-1}\ K^{-1}$; $\lambda^{eff}{}_{RT} = 3.02\ Wm^{-1}\ K^{-1}$ and keeping λ_{ph} constant). Open diamonds indicate the respective ZT_{appr} data

2 Conclusive Remarks

In this review, we have tried to highlight the advancements in thermoelectric materials and possible strategies to improve the thermoelectric efficiency of the traditional and newly designed TE materials. Further investigations are carried out on higher ZT enhancement of TE coefficients like S, σ at the same time the κ must be kept low values. The later has been found to be ultra-low in some 2D materials yet to be realized experimentally. It opens the window for the researchers to design the new strategies for practically synthesizable nanostructure materials. Hence, novel techniques to stabilize higher ZT in nanostructured metastable alloys like $Fe_2V_{0.8}W_{0.2}Al$ Heusler thin film and the TE application demands practically need to be acquired at elevated temperature for broader scope of this technology. Upcoming TE devices developed from these nanomaterials sought to be extensively used in cooling/refrigeration/air-conditioning applications at large scale and to launch a consistent, well-organized, eco-friendly energy consumption on our planet earth.

References

1. Snyder, G.J., Toberer, E.S.: Complex thermoelectric materials. Nat. Mater. **7**, 105–114 (2008)
2. Seebeck, T.J.: Magnetische polarisation der metalle und erze durch temperatur-differenz (magnetic polarization of metals and minerals by temperature differences), Abhandlungen der Königlichen Akademie der Wissenschaften zu Berlin (Treatises of the Royal Academy of Sciences in Berlin), pp. 265–373 (1825)
3. Seebeck, T.J.: Ueber die magnetische polarisation der metalle und erze durch temperatur-differenz (on the magnetic polarization of metals and minerals by temperature differences). Annalen der Physik und Chemie **6**, 133–160 (1826)
4. Peltier, J.C.A.: Nouvelles expériences sur la caloricité des courants électrique (new experiments on the heat effects of electric currents). Annales de Chimie et de Physique **56**, 371–386 (1834)
5. Riffat, S.B., Ma, X.L.: Thermoelectrics: a review of present and potential applications. Appl. Therm. Eng. **23**, 913–935 (2003)
6. Tritt, T.M., Subramanian, M.A.: Thermoelectric materials, phenomena, and applications: a bird's eye view. MRS. Bull. **31**, 188 (2006)
7. Zhu, T., Liu, Y., Fu, C., Heremans, J.P., Snyder, J.G., Zhao, X.: Compromise and synergy in high-efficiency thermoelectric materials. Adv. Mater. **29**, 1605884 (2017)
8. Vining, C.B.: An inconvenient truth about thermoelectrics. Nat. Mater. **8**, 83 (2009)
9. Ibrahim, E.A., Szybist, J.P., Parks, J.E.: Enhancement of automotive exhaust heat recovery by thermoelectric devices. P. I. Mech. Eng. Part D J. Automob. Eng. **224**, 1097–1111 (2010)
10. Li, M., Xu, S., Chen, Q., Zheng, L.: Thermoelectric-generator-based DC–DC conversion networks for automotive applications. J. Electron. Mater. **40**, 1136–1143 (2011)
11. Schierle-Arndt, K., Hermes, W.: Thermoelektrik. Chem. Unserer. Zeit. **47**, 92 (2013)
12. Kraemer, D., et al.: Concentrating solar thermoelectric generators with a peak efficiency of 7.4%. Nat. Energy, **1**, 16153 (2016)
13. Kraemer, D., et al.: High-performance flat-panel solar thermoelectric generators with high thermal concentration. Nat. Mater. **10**, 532–538 (2011)
14. Friedensen, V.P.: Space nuclear power: Technology, policy, and risk considerations in human missions to Mars. Acta Astronaut. **42**, 395 (1998)

15. Yang, J.H., Caillat, T.: Thermoelectric materials for space and automotive power generation. MRS Bulltin **31**, 224 (2006)
16. O'Brien, R.C., Ambrosi, R.M., Bannister, N.P., Howe, S.D., Atkinson, H.V.: Safe radioisotope thermoelectric generators and heat sources for space applications. J. Nucl. Mater. **389**, 506–521 (2008)
17. He, J., Tritt, T.M.: Advances in thermoelectric materials research: looking back and moving forward. Science **357**, 6358 (2017)
18. Bahk, J.H., Fang, H., Yazawa, K., Shakouri, A.: Flexible thermoelectric materials and device optimization for wearable energy harvesting. J. Mater. Chem. C **3**, 10362–10374 (2015)
19. Biswas, K., et al.: High-performance bulk thermoelectrics with all-scale hierarchical architectures. Nature **489**, 414–418 (2012)
20. Bell, L.E.: Cooling, heating, generating power, and recovering waste heat with thermoelectric systems. Science **321**, 1457–1461 (2008)
21. Yang, J., Caillat, T.: Thermoelectric materials for space and automotive power generation. MRS Bull. **31**, 224–229 (2006)
22. Chen, Z.-G., Han, G., Yang, L., Cheng, L., Zou, J.: Nanostructured thermoelectric materials: current research and future challenge. Prog. Nat. Sci. Mater. Int. **22**, 535–549 (2012)
23. Pichanusakorn, P., Bandaru, P.: Nanostructured thermoelectrics. Mater. Sci. Eng. R. Rep. **67**, 19–63 (2010)
24. Zebarjadi, M., Esfarjani, K., Dresselhaus, M.S., Ren, Z.F., Chen, G.: Perspectives on thermoelectrics: from fundamentals to device applications. Energy Environ. Sci. **5**, 5147–5162 (2012)
25. Sootsman, J.R., Chung, D.Y., Kanatzidis, M.G.: New and old concepts in thermoelectric materials. Angew. Chem. Int. Ed. **48**, 8616–8639 (2009)
26. Vineis, C.J., Shakouri, A., Majumdar, A., Kanatzidis, M.G.: Nanostructured thermoelectrics: big efficiency gains from small features. Adv. Mater. **22**, 3970–3980 (2010)
27. Vaqueiro, P., Powell, A.V.: Recent developments in nanostructured materials for high-performance thermoelectrics. J. Mater. Chem. **20**, 9577–9584 (2010)
28. Bux, S.K., Fleurial, J.P., Kaner, R.B.: Nanostructured materials for thermoelectric applications. Chem. Commun. **46**, 8311–8324 (2010)
29. Minnich, A.J., Dresselhaus, M.S., Ren, Z.F., Chen, G.: Bulk nanostructured thermoelectric materials: current research and future prospects. Energy Environ. Sci. **2**, 466–479 (2009)
30. Kanatzidis, M.G.: Nanostructured thermoelectrics: the new paradigm? Chem. Mater. **22**, 648–659 (2009)
31. Dresselhaus, M.S., et al.: New directions for low-dimensional thermoelectric materials. Adv. Mater. **19**, 1043–1053 (2007)
32. Dresselhaus, M., Dresselhaus, G., Sun, X., Zhang, Z., Cronin, S., Koga, T.: Low-dimensional thermoelectric materials. Phys. Solid State **41**, 679–682 (1999)
33. Rao, A.M., Ji, X., Tritt, T.M.: Properties of nanostructured one dimensional and composite thermoelectric materials. MRS Bull. **31**, 218–223 (2006)
34. Hochbaum, A.I., et al.: Enhanced thermoelectric performance of rough silicon nanowires. Nature **451**, 163–167 (2008)
35. Boukai, A.I., Bunimovich, Y., Tahir-Kheli, J., Yu, J.-K., Goddard, W.A., III., Heath, J.R.: Silicon nanowires as efficient thermoelectric materials. Nature **451**, 168–171 (2008)
36. Hicks, L.D., Dresselhaus, M.S.: Thermoelectric figure of merit of a one-dimensional conductor. Phys. Rev. B **47**, 16631–16634 (1993)
37. Chen, G.: Thermal conductivity and ballistic-phonon transport in the cross plane direction of superlattices. Phys. Rev. B **57**, 14958–14973 (1998)
38. Venkatasubramanian, R., Siivola, E., Colpitts, T., O'Quinn, B.: Thin-film thermoelectric devices with high room-temperature figures of merit. Nature **413**, 597–602 (2001)
39. Harman, T.C., Taylor, P.J., Walsh, M.P., LaForge, B.E.: Quantum dot superlattice thermoelectric materials and devices. Science **297**, 2229–2232 (2002)
40. Böttner, H., Chen, G., Venkatasubramanian, R.: Aspects of thin-film superlattice thermoelectric materials, devices, and applications. MRS Bull. **31**, 211–217 (2006)

41. Heremans, J.P., Thrush, C.M., Morelli, D.T.: Thermopower enhancement in lead telluride nanostructures. Phys. Rev. B **70**, 115334 (2004)
42. Lee, S.-M., Cahill, D.G., Venkatasubramanian, R.: Thermal conductivity of Si-Ge superlattices. Appl. Phys. Lett. **70**, 2957–2959 (1997)
43. Yang, R., Chen, G.: Thermal conductivity modeling of periodic two-dimensional nanocomposites. Phys. Rev. B **69**, 195316 (2004)
44. Medlin, D.L., Snyder, G.J.: Interfaces in bulk low thermoelectric materials: a review for current opinion in colloid and interface science. Curr. Opin. Colloid Interface Sci. **14**, 226–235 (2009)
45. Lan, Y., Ren, Z.: Ch.11. In: Li, Q. (ed.) Nanomaterials for Sustainable Energy, NanoScience and Technology. Springer International Publishing, Switzerland (2016)
46. Wang, X.W., et al.: Enhanced thermoelectric figure of merit in nanostructured n-type silicon germanium bulk alloy. Appl. Phys. Lett. **93**, 193121 (2008)
47. Joshi, G., et al.: Enhanced thermoelectric figure-of-merit in nanostructured p-type silicon germanium bulk alloys. Nano Lett. **8**, 4670–4674 (2008)
48. Yan, X., et al.: Enhanced thermoelectric figure of merit of p-type Half-Heuslers. Nano Lett. **11**, 556–560 (2011)
49. Zhu, G.H., et al.: Effect of selenium deficiency on the thermoelectric properties of n-type In4Se3−x compounds. Phys. Rev. B **83**, 115201 (2011)
50. Zhao, H., et al.: High thermoelectric performance of MgAgSb-based materials. Nano Energy **7**, 97–103 (2014)
51. Morelli, D.T., et al.: Low-temperature transport properties of p-type $CoSb_3$. Phys. Rev. B **51**, 9622 (1995)
52. Caillat, T., Borshchevsky, A., Fleurial, J.P.: Properties of single crystalline semiconducting $CoSb_3$. J. Appl. Phys. **80**, 4442 (1996)
53. Nolas, G.S., Slack, G.A., Schujman, S.B.: Recent Trends in Thermoelectric Materials Research I, vol. 69, p. 255. Academic Press Inc, San Diego (2001)
54. Rowe, D.M. (ed.): CRC Handbook of Thermoelectrics. CRC Press, Boca Raton, FL (1995)
55. Nolas, G.S., Morelli, D.T., Tritt, T.M.: Skutterudites: a phonon-glass-electron crystal approach to advanced thermoelectric energy conversion applications. Annu. Rev. Mater. Sci. **29**, 89–126 (1999)
56. Sales, B.C., Mandrus, D., Williams, R.K.: Filled skutterudite antimonides: a new class of thermoelectric materials. Science **272**, 1325–1328 (1996)
57. Sales, B.C., Mandrus, D., Chakoumakos, B.C., Keppens, V., Thompson, J.R.: Filled skutterudite antimonides: electron crystals and phonon glasses. Phys. Rev. B **56**, 15081 (1997)
58. Nolas, G.S., Cohn, J.L., Slack, G.A., Schujman, S.B.: Semiconducting Ge clathrates: promising candidates for thermoelectric applications. Appl. Phys. Lett. **73**, 178 (1998)
59. Blake, N.P., Mollnitz, L., Kresse, G., Metiu, H.: Why clathrates are good thermoelectrics: a theoretical study of Sr8Ga16Ge30. J. Chem. Phys. **111**, 3133 (1999)
60. Iversen, B.B., et al.: Why are clathrates good candidates for thermoelectric materials? J. Solid State Chem. **149**, 455–458 (2000)
61. Kauzlarich, S.M., Brown, S.R., Snyder, G.J.: Zintl phases for thermoelectric devices. Dalton Trans. **21**, 2099–2107 (2007)
62. Hicks, L.D., Dresselhaus, M.S.: Effect of quantum-well structures on the thermoelectric figure of merit. Phys. Rev. B **47**, 12727 (1993)
63. Chen, G.: Thermal conductivity and ballistic-phonon transport in the cross-plane direction of superlattices. Phys. Rev. B **57**, 14958 (1998)
64. Heremans, J.P., Thrush, C.M., Morelli, D.T., Wu, M.C.: Thermoelectric power of bismuth nanocomposites. Phys. Rev. Lett. **88**, 216801 (2002)
65. Harman, T.C., Walsh, M.P., Laforge, B.E., Turner, G.W.: Nanostructured thermoelectric materials. J. Electron. Mater. **34**, L19–L22 (2005)
66. Harman, T.C., Reeder, R.E., Walsh, M.P., LaForge, B.E., Hoyt, C.D., Turner, G.W.: High electrical power density from PbTe-based quantum-dot superlattice unicouple thermoelectric devices. Appl. Phys. Lett. **88**, 243504 (2006)

67. Vineis, C.J., et al.: Carrier concentration and temperature dependence of the electronic transport properties of epitaxial PbTe and PbTe/PbSe nanodot superlattices. Phys. Rev. B **77**, 235202 (2008)
68. Pei, Y., Shi, X., LaLonde, A., Wang, H., Chen, L., Snyder, G.J.: Convergence of electronic bands for high performance bulk thermoelectrics. Nature **473**, 66–69 (2011)
69. Baxter, J., et al.: Nanoscale design to enable the revolution in renewable energy. Energy Environ. Sci. **2**, 559–588 (2009)
70. Moshwan, R., Yang, L., Zou, J., Chen, Z.G.: Eco-friendly SnTe thermoelectric materials: progress and future challenges. Adv. Funct. Mater. **27**, 1703278 (2017)
71. Tan, G., et al.: High thermoelectric performance of p-Type SnTe via a synergistic band engineering and nanostructuring approach. J. Am. Chem. Soc. **136**, 7006–7016 (2014)
72. Tan, G., et al.: Codoping in SnTe: enhancement of thermoelectric performance through synergy of resonance levels and band convergence. J. Am. Chem. Soc. **137**, 5100–5112 (2015)
73. Tan, G., et al.: Valence band modification and high thermoelectric performance in SnTe heavily alloyed with MnTe. J. Am. Chem. Soc. **137**, 11507–11516 (2015)
74. Tan, G., et al.: Extraordinary role of Hg in enhancing the thermoelectric performance of p-type SnTe. Energy Environ. Sci. **8**, 267–277 (2015)
75. Yang, L., Chen, Z.G., Dargusch, M.S., Zou, J.: High performance thermoelectric materials: progress and their applications. Adv. Energy Mater. **8**, 1701797 (2018)
76. Zhao, L.D., et al.: Ultralow thermal conductivity and high thermoelectric figure of merit in SnSe crystals. Nature **508**, 373–377 (2014)
77. Zhao, L.D., et al.: Ultrahigh power factor and thermoelectric performance in hole-doped single-crystal SnSe. Science **351**, 141–144 (2016)
78. Peng, K., et al.: Broad temperature plateau for high ZTs in heavily doped p-type SnSe single crystals. Energy Environ. Sci. **9**, 454-460 (2016)
79. DiSalvo, F.J.: Thermoelectric cooling and power generation. Science **285**, 703–706 (1999)
80. Chen, Z.G., Han, G., Yang, L., Cheng, L., Zou, J.: Nanostructured thermoelectric materials: current research and future challenge. Prog. Nat. Sci. **22**, 535–549 (2012)
81. Wood, C.: Materials for thermoelectric energy-conversion. Rep. Prog. Phys. **51**, 459–539 (1988)
82. Szczech, J.R., Higgins, J.M., Jin, S.: Enhancement of the thermo- electric properties in nanoscale and nanostructured materials. J. Mater. Chem. **21**, 4037–4055 (2011)
83. Rowe, D.M., Bunce, R.W.: The thermoelectric properties of heavily doped hot-pressed germanium-silicon alloys. J. Phys. D Appl. Phys. **2**, 1497 (1969)
84. Benjamin, J.S.: Mechanical alloying. Sci. Am. **234**, 40–49 (1976)
85. Suryanarayana, C.: Mechanical alloying and milling. Prog. Mater Sci. **46**, 1–184 (2001)
86. Loeff, P., Bakker, H.: Amorphous gold-lanthanum alloy prepared by ball milling. Scr. Metall. **22**, 401–404 (1988)
87. Basset, D., Matteazzi, P., Miani, F.: Designing a high energy ball-mill for synthesis of nanophase materials in large quantities. Mater. Sci. Eng. A **168**, 149–152 (1993)
88. Yamada, K., Koch, C.C.: The influence of mill energy and temperature on the structure of the TiNi intermetallic after mechanical attrition. J. Mater. Res. **8**, 1317–1326 (1993)
89. Gusev, A.I., Rempel, A.A.: Nanocrystalline Materials. Cambridge International Science Publishing, Cambridge (2004)
90. Umemoto, M.: Preparation of thermoelectric β-FeSi2 doped with Al and Mn by mechanical alloying (overview). Mater. Trans. JIM **36**, 373 (1995)
91. Davis, R.M., Koch, C.C.: Mechanical alloying of brittle components: silicon and germanium. Scr. Metall. **21**, 305–310 (1987)
92. Bouad, N., Marin-Ayral, R.M., Tedenac, J.C.: Mechanical alloying and sintering of lead telluride. J. Alloy. Compd. **297**, 312–318 (2000)
93. Kishimoto, K., Koyanagi, T.: Preparation of sintered degenerate n-type PbTe with a small grain size and its thermoelectric properties. J. Appl. Phys. **92**, 2544 (2002)
94. Bouad, N., Record, M.C., Tedenac, J.C., Marin-Ayral, R.M.: Mechanical alloying of a thermoelectric alloy: $Pb_{0.65}Sn_{0.35}Te$. J. Solid State Chem. **177**, 221–226 (2004)

95. Zhang, Q., et al.: High thermoelectric performance by resonant dopant indium in nanostructured SnTe. Proc. Natl. Acad. Sci. USA **110**, 13261–13266 (2013)
96. Liu, W., et al.: Bi_2S_3 nanonetwork as precursor for improved thermoelectric performance. Nano Energy **4**, 113–122 (2014)
97. Poudel, B., et al.: High-thermoelectric performance of nanostructured bismuth antimony telluride bulk alloys. Science **320**, 634–638 (2008)
98. Pierrat, P., Dauscher, A., Lenoir, B., Martin-Lopez, R., Scherrer, H.: Preparation of the $Bi_8Sb_{32}Te_{60}$ solid solution by mechanical alloying. J. Mater. Sci. **32**, 3653–3657 (1997)
99. Kim, H.C., Oh, T.S., Hyun, D.B.: Thermoelectric properties of the p-type Bi_2Te_3–Sb_2Te_3–Sb_2Se_3 alloys fabricated by mechanical alloying and hot pressing. J. Phys. Chem. Solids **61**, 743–749 (2000)
100. Schilz, J., Riffel, M., Pixius, K., Meyer, H.J.: Synthesis of thermoelectric materials by mechanical alloying in planetary ball mills. Powder Technol. **105**, 149–154 (1999)
101. Yang, J.Y., et al.: Synthesis of $CoSb_3$ skutterudite by mechanical alloying. J. Alloy. Compd. **375**, 229–232 (2004)
102. Ma, Y., et al.: Enhanced thermoelectric figure-of-merit in p-type nanostructured bismuth antimony tellurium alloys made from elemental chunks. Nano Lett. **8**, 2580–2584 (2008)
103. Kanatzia, A., Papageorgiou, C., Lioutas, C., Kyratsi, T.: Design of ball milling experiments on Bi_2Te_3 thermoelectric material. J. Electron. Mater. **42**, 1652–1660 (2013)
104. Yan, X., et al.: Experimental studies on anisotropic thermoelectric properties and structures of n-type $Bi_2Te_{2.7}Se_{0.3}$. Nano Lett. **10**, 3373–3378 (2010)
105. Liu, W.-S., et al.: Thermoelectric property studies on Cu-doped n-type $Cu_xBi_2Te_{2.7}Se_{0.3}$ nanocomposites. Adv. Energy Mater. **1**, 577–587 (2011)
106. Zhu, G., et al.: The effect of secondary phase on thermoelectric properties of Zn_4Sb_3 compound. Nano Energy **2**, 1172–1178 (2013)
107. Sui, J., et al.: Effect of Cu concentration on thermoelectric properties of nanostructured p-type $MgAg_{0.97-x}Cu_x$ $Sb_{0.99}$. Acta Mater. **87**, 266–272 (2015)
108. Shuai, J., et al.: Study on thermoelectric performance by Na doping in nanostructured $Mg_{1-x}Na_xAg_{0.97}Sb_{0.99}$. Nano Energy **11**, 640–646 (2015)
109. Zhang, Q., et al.: Increased thermoelectric performance by Cl doping in nanostructured $AgPb_{18}SbSe_{20-x}$ Clx. Nano Energy **2**, 1121–1127 (2013)
110. Koirala, M., et al.: Nanostructured $YbAgCu_4$ for potentially cryogenic thermoelectric cooling. Nano Lett. **14**, 5016–5020 (2014)
111. Yang, J., et al.: Solubility study of Yb in n-type skutterudites $Yb_xCo_4Sb_{12}$ and their enhanced thermoelectric properties. Phys. Rev. B **80**, 115329 (2009)
112. Dahal, T., et al.: Thermoelectric property enhancement in Yb-doped n-type skutterudites $Yb_xCo_4Sb_{12}$. Acta Mater. **75**, 316–321 (2014)
113. Dahal, T., et al.: Substitution of antimony by tin and tellurium in n-type skutterudites $CoSb_{2.8}Sn_xTe_{0.2-x}$. J. Miner. Met Mater. Soc. **66**, 2282–2287 (2014)
114. Dahal, T., Jie, Q., Lan, Y., Guo, C., Ren, Z.: Thermoelectric performance of Ni compensated cerium and neodymium double filled p-type skutterudites. Phys. Chem. Chem. Phys. **16**, 18170–18175 (2014)
115. Dahal, T., et al.: Effect of triple fillers in thermoelectric performance of p-type skutterudites. J. Alloy. Compd. **623**, 104–108 (2015)
116. Dahal, T., et al.: Thermoelectric and mechanical properties on misch metal filled p-type skutterudites $Mn_{0.9}Fe_{4-x}Co_xSb_{12}$. J. Appl. Phys. **117**, 055101 (2015)
117. Raihan, O., et al.: Parametric analysis of ball milling condition on thermoelectric performance of $Bi_{0.6}FeCo_3Sb_{12}$ skutterudite. Mater. Res. Express **5**, 105008 (2018)
118. May, A.F., Fleurial, J.P., Snyder, G.J.: Thermoelectric performance of lanthanum telluride produced via mechanical alloying. Phys. Rev. B **78**, 125205 (2008)
119. Zhu, G.H., et al.: Increased phonon scattering by nanograins and point defects in nanostructured silicon with a low concentration of germanium. Phys. Rev. Lett. **102**, 196803 (2009)

120. Bathula, S., et al.: Enhanced thermoelectric figure-of-merit in spark plasma sintered nanostructured n-type SiGe alloys. Appl. Phys. Lett. **101**, 213902 (2012)
121. Bashir, M.B.A., et al.: Enhancement of thermoelectric properties of Co_4Sb_{12} Skutterudite by Al and La double filling. J. Solid State Chem. **284**, 121205 (2020)
122. Prado-Gonjal, J., Vaqueiro, P., Nuttall, C., Potter, R., Powell, A.V.: Enhancing the thermoelectric properties of single and double filled p-type skutterudites synthesized by an up-scaled ball milling process. J Alloys Compd. **695**, 3598–3604 (2017)
123. Li, J., Li, S., Wang, Q., Wang, L., Liu, F., Ao, W.: Effect of Ce-doping on thermoelectric properties in PbTe alloys prepared by spark plasma sintering. J. Electron. Mater. **40**, 2063 (2011)
124. Yang, J., Fan, X., Chen, R., Zhu, W., Bao, S., Duan, X.: Consolidation and thermoelectric properties of n-type bismuth telluride based materials by mechanical alloying and hot pressing. J. Alloy. Compd. **416**, 270–273 (2006)
125. Sridhar, K., Chattopadhyay, K.: Synthesis by mechanical alloying and thermoelectric properties of Cu_2Te. J. Alloy. Compd. **264**, 293–298 (1998)
126. Martin-Lopez, R., Dauscher, A., Scherrer, H., Hejtmanek, J., Kenzari, H., Lenoir, B.: Thermoelectric properties of mechanically alloyed Bi-Sb alloys. Appl. Phys. A **68**, 597–602 (1999)
127. Zevalkink, A., Swallow, J., Snyder, G.J.: Thermoelectric properties of Mn-doped $Ca_5Al_2Sb_6$. J Electron. Mater. **41**, 813–818 (2012)
128. Zevalkink, A., Toberer, E.S., Bleith, T., Flage-Larsen, E., Snyder, G.J.: Improved carrier concentration control in Zn-doped $Ca_5Al_2Sb_6$. J. Appl. Phys. **110**, 013721 (2011)
129. Johnson, S.I., Zevalkink, A., Snyder, G.J.: Improved thermoelectric properties in Zn-doped $Ca_5Ga_2Sb_6$. J. Mater Chem A. **1**, 4244–4249 (2013)
130. Zevalkink, A., Zeier, W.G., Cheng, E., Snyder, J., Fleurial, J.-P., Bux, S.: Nonstoichiometry in the Zintl phase $Yb_{1-\delta}Zn_2Sb_2$ as a route to thermoelectric optimization. Chem Mater. **26**, 5710–5717 (2014)
131. Chanakian, S., Zevalkink, A., Aydemir, U.: Enhanced thermoelectric properties of $Sr_5In_2Sb_6$ via Zn-doping. J. Mater Chem A. **3**, 10289–10295 (2015)
132. Tamaki, H., Sato, H.K., Kanno, T.: Isotropic conduction network and defect chemistry in $Mg_{3+\delta}Sb_2$-based layered Zintl compounds with high thermoelectric performance. Adv Mater. **28**, 10182–10187 (2016)
133. Santos, R., Nancarrow, M., Dou, S.X., Aminorroaya Yamini, S.: Thermoelectric performance of n-type Mg_2Ge. Sci Rep. **7**, 3988 (2017)
134. Fan, W., et al.: Enhancing the zT value of bidoped $Mg_2Si_{0.6}Sn_{0.4}$ materials through reduction of bipolar thermal conductivity. ACS Appl. Mater. Interfaces **9**, 28635–28641 (2017)
135. Khan, T.T., Mahmud, I., Ur, S.-C.: Synthesis and thermoelectric properties of the B-site substituted $SrTiO_3$ with vanadium. Korean J. Mater. Res. **27**, 416–421 (2017)
136. Khan, T.T., Ur, S.-C.: Thermoelectric properties of the yttrium doped ceramic oxide $SrTiO_3$. J. Korean Phys. Soc. **70**, 93–97 (2017)
137. Jiang, Q., Yang, J., Xin, J., Zhou, Z., Zhang, D., Yan, H.: Carriers concentration tailoring and phonon scattering from n-type zinc oxide (ZnO) nanoinclusion in p- and n-type bismuth telluride (Bi_2Te_3): leading to ultra low thermal conductivity and excellent thermoelectric properties. J. Alloys Compd. **694**, 864–868 (2017)
138. Löhnert, R., Stelter, M., Töpfer, J.: Evaluation of soft chemistry methods to synthesize Gd-doped $CaMnO_{3-\delta}$ with improved thermoelectric properties. Mater. Sci. Eng. B. **223**, 185–193 (2017)
139. Zhao, X.B., Ji, X.H., Zhang, Y.H., Zhu, T.J., Tu, J.P., Zhang, X.B.: Bismuth telluride nanotubes and the effects on the thermoelectric properties of nanotube-containing nanocomposites. Appl. Phys. Lett. **86**, 062111 (2005)
140. Gothard, N., Ji, X., He, J., Tritta, T.M.: Thermoelectric and transport properties of n-type Bi_2Te_3 nanocomposites. J. Appl. Phys. **103**, 054314 (2008)
141. Ni, H.L., Zhao, X.B., Zhu, T.J., Ji, X.H., Tu, J.P.: Synthesis and thermoelectric properties of Bi2Te3 based nanocomposites. J. Alloy. Compd. **397**, 317–321 (2005)

142. Wang, W., Wang, W., Poudel, B., Yang, J., Wang, D.Z., Ren, Z.F.: High-yield synthesis of single-crystalline antimony telluride hexagonal nanoplates using a solvothermal approach. J. Am. Chem. Soc. **127**, 13792–13793 (2005)
143. Yu, S.H., et al.: A new low temperature one-step route to metal chalcogenide semiconductors: PbE, Bi_2E_3 (E = S, Se, Te). J. Mater. Chem. **8**, 1949–1951 (1998)
144. Mi, J.L., Zhao, X.B., Zhu, T.J., Tu, J.P., Cao, G.S.: Solvothermal synthesis and electrical transport properties of skutterudite $CoSb_3$. J. Alloy. Compd. **417**, 269–272 (2006)
145. Mi, J.L., Zhao, X.B., Zhu, T.J., Tu, J.P.: In-situ solvothermal and hot pressing preparation of micro-nano composite n-type $CoSb_3$ and its thermoelectric properties. J. Inorg. Mater. **23**, 715–718 (2008)
146. Makongo, J.P.A., et al.: Simultaneous large enhancements in thermopower and electrical conductivity of bulk nanostructured half-Heusler alloys. J. Am. Chem. Soc. **133**, 18843–18852 (2011)
147. Fan, F.J., et al.: Colloidal synthesis of $Cu_2CdSnSe_4$ nanocrystals and hot pressing to enhance the thermoelectric figure-of-merit. J. Am. Chem. Soc. **133**, 15910–15913 (2011)
148. Wang, D.B., et al.: Preparation and characterization of wire-like Sb_2Se_3 and flake-like Bi_2Se_3 nano crystals. J. Cryst. Growth **253**, 445–451 (2003)
149. Deng, Y., et al.: Solvothermal preparation and characterization of nanocrystalline Bi_2Te_3 powders with different morphology. J. Phys. Chem. Solid **63**, 2119–2121 (2002)
150. Wang, W.Z., et al.: High-yield synthesis of single-crystalline antimony telluride nano plate using a solvothermal approach. J. Am. Chem. Soc. **127**, 13792–21379 (2005)
151. Zhao, X.B., Sun, T., Zhu, T.J., Tu, J.P.: In-situ investigation and effect of additives on low temperature aqueous chemical synthesis of Bi_2Te_3 nanocapsules. J. Chem. Mater. **15**, 1621–1625 (2005)
152. Yu, H., Gibbons, P.C., Buhro, W.E.: Bismuth, telluride, and bismuth telluride nanowires. J. Mater. Chem. **14**, 595–602 (2004)
153. Urban, J.J., Talapin, D.V., Shevchenko, E.V., Murray, C.B.: Self-assembly of PbTe Quantum dots into nano crystal supper lattice and Glass Film. J. Am. Chem. Soc. **128**, 3248–3255 (2006)
154. Wang, W.Z., Poudel, B., Wang, D.Z., Ren, Z.F.: Synthesis of PbTe nanoboxes using a solvothermal technique. Adv. Mater. **17**, 2110–2114 (2005)
155. Tai, G.A., Zhou, B., Guo, W.L.: Structure characterization and thermoelectric transport properties of uniform single crystalline Lead telluride nanowire. J. Phys. Chem. C **112**, 11314–11318 (2008)
156. Gothard, N., Spowart, J.E., Tritt, T.M.: Thermal conductivity reduction in fullerene-enriched p-type bismuth telluride composites. Phys. Status Solidi A **207**, 157–162 (2007)
157. Schultz, J.M., McHugh, J.P., Tiller, W.A.: Effects of heavy deformation and annealing on electrical properties of Bi2Te3. J. Appl. Phys. **33**, 2443–2450 (1962)
158. Oh, T.S., Hyun, D.B., Kolomoets, N.V.: Thermoelectric properties of the hot-pressed (Bi, $Sb)_2$(Te, $Se)_3$ alloys. Scripta Mater. **42**, 849–854 (2000)
159. Liu, W., Ren, Z., Chen, G.: Thermoelectric Nanomaterials Book, Chapter 11, Springer Series in Materials Science, vol. 182
160. Xiao, F., Hangarter, C., Yoo, B.Y., Rheem, Y.W., Lee, K.H., Myung, N.V.: Recent progress in electrodeposition of thermoelectric thin films and nanostructures. Electrochim. Acta **53**, 8103–8117 (2008)
161. Snyder, G.J., Lim, J.R., Huang, C.K., Fleurial, J.P.: Thermoelectric microdevice fabricated by a MEMS-like electrochemical process. Nat. Mater. **2**, 528 (2003)
162. Chen, L.J., Hu, H.N., Li, Y.X., Chen, G.F., Yu, S.Y., Wu, G.H.: Ordered $CoSb_3$ nanowire arrays synthesized by electrodeposition. Chem. Lett. **35**, 170–171 (2006)
163. Martin-Gonzalez, M., Prieto, A.L., Gronsky, R., Sands, T., Stacy, A.M.: High-density 40 nm diameter Sb-Rich $Bi_{2-x}Sb_xTe_3$ nanowire arrays. Adv. Mater. **15**, 1003–1006 (2003)
164. Jin, C.G., et al.: Electrochemical fabrication of large-area, ordered Bi_2Te_3 nanowire array. J. Phys. Chem. B **108**, 1844–1847 (2004)

165. Jin, C.G., Zhang, G.Q., Qian, T., Li, X.G., Yao, Z.: Large-area Sb_2Te_3 nanowire arrays. J. Phys. Chem. B **109**, 1430–1432 (2005)
166. Martin-Gonzalez, M., Snyder, G.J., Prieto, A.L., Gronsky, R., Sands, T., Stacy, A.M.: Direct Electrodeposition of highly dense 50 nm $Bi_2Te_{3-y}Se_y$ nanowire arrays. Nano Lett. **3**, 973 (2003)
167. Liu, W.F., Cai, W.L., Yao, L.Z.: Electrochemical deposition of well-ordered single-crystal PbTe nanowire arrays. Chem. Lett. **36**, 1362 (2007)
168. Wang, W., Qu, J.F., Lu, X.L., Zhang, G.Q., Li, G., Li, X.G.: Electrochemical Fabrication of Bi_xTe_{1-x} ($0.4 \leq x \leq 0.7$) Nanowire Arrays. Mater. Sci. Forum **2171**, 546–549 (2007)
169. Li, L., Yang, Y.W., Huang, X.H., Li, G.H., Zhang, L.D.: Pulsed electrodeposition of single-crystalline Bi_2Te_3 nanowire arrays. Nanotechnology **17**, 1706 (2006)
170. Trahey, L., Becker, C.R., Stacy, A.M.: Electrodeposited bismuth telluride nanowire arrays with uniform growth fronts. Nano Lett. **7**, 2535 (2007)
171. Li, L., Yang, Y.W., Huang, X.H., Li, G.H., Ang, R., Zhang, L.D.: Fabrication and electronic transport properties of Bi nanotube arrays. Appl. Phys. Lett. **88**, 103119 (2006)
172. Li, X.H., Zhou, B., Pu, L., Zhu, J.J.: Electrodeposition of Bi_2Te_3 and Bi_2Te_3 derived alloy nanotube arrays. Cryst. Growth Des. **8**, 771 (2008)
173. Zhou, B., Li, X.H., Zhu, J.J.: Controllable synthesis of one-dimensional chinelike superstructures of homogeneous $Bi_{100-x}Sb_x$ alloys via a template-free electrodeposition. Cryst. Growth Des. **7**, 2276 (2007)
174. Xiao, F., Yoo, B.Y., Bozhilov, K.N., Lee, K.H., Myung, N.V.: Electrodeposition of single-crystal cubes of lead telluride on polycrystalline gold substrate. J. Phys. Chem. C **111**, 11397 (2007)
175. Menke, E.J., Li, Q., Penner, R.M.: Bismuth telluride (Bi_2Te_3) nanowires synthesized by cyclic electrodeposition/stripping coupled with step edge decoration. Nano Lett. **4**, 2009 (2004)
176. Xue, F.H., Fei, G.T., Wu, B., Cui, P., Zhang, L.D.: Direct electrodeposition of highly dense Bi/Sb superlattice nanowire arrays. J. Am. Chem. Soc. **127**, 15348 (2005)
177. Yoo, B., Xiao, F., Bozhilov, K.N., Herman, J., Ryan, M.A., Myung, N.V.: Electrodeposition of thermoelectric superlattice nanowires. Adv. Mater. **19**, 296 (2007)
178. Wang, W., Zhang, G.Q., Li, X.G.: Manipulating growth of thermoelectric Bi_2Te_3/Sb multilayered nanowire arrays. J. Phys. Chem. C **112**, 15190 (2008)
179. Wang, W., Lu, X.L., Zhang, T., Zhang, G.Q., Jiang, W.J., Li, X.G.: Facile synthesis of a hierarchical PbTe flower-like nanostructure and its shape evolution process guided by a kinetically controlled regime. J. Am. Chem. Soc. **129**, 6702 (2007)
180. Dresselhaus, M.S., et al.: Materials and technologies for direct thermal-to-electric energy conversion. In: Yang, J., Hogan, T.P., Funahashi, R., Nolas, G.S. (eds.) MRS Symposium Proceedings, vol. 886, p. 3. Pittsburgh, PA (2005)
181. Benelmekki, M.: Nanomaterials: The Original Product of Nanotechnology Book, Chapter 2. IOP Publishing, Bristol (2019)
182. Johnsen, S., et al.: Nanostructures boost the thermoelectric performance of PbS. J. Am. Chem. Soc. **133**, 3460 (2011)
183. He, J.Q., et al.: Anomalous electronic transport in dual-nanostructured lead telluride. J. Am. Chem. Soc. **133**, 8786 (2011)
184. Androulakis, J., Todorov, I., He, J., Chung, D., Dravid, V., Kanatzidis, M.G.: Thermoelectrics from abundant chemical elements: high-performance nanostructured PbSe–PbS. J. Am. Chem. Soc. **133**, 10920–10927 (2011)
185. Girard, S.N., et al.: High performance Na-doped PbTe–PbS thermoelectric materials: electronic density of states modification and shape-controlled nanostructures. J. Am. Chem. Soc. **133**, 16588–16597 (2011)
186. Biswas, K., et al.: High thermoelectric figure of merit in nanostructured p-type PbTe–MTe (M= Ca, Ba). Energy Environ. Sci. **4**, 4675–4684 (2011)
187. Zhao, L., et al.: High performance thermoelectrics from earth-abundant materials: enhanced figure of merit in PbS by second phase nanostructures. J. Am. Chem. Soc. **133**, 20476–20487 (2011)

188. He, J., Androulakis, J., Kanatzidis, M.G., Dravid, V.P.: Seeing is believing: weak phonon scattering from nanostructures in alkali metal-doped lead telluride. Nano Lett. **12**, 343–347 (2012)
189. Hsu, K.F., et al.: Cubic $AgPb_mSbTe_{2+m}$: bulk thermoelectric materials with high figure of merit. Science **303**, 818−821 (2004)
190. Cook, B.A., Kramer, M.J., Harringa, J.L., Han, M.K., Chung, D.Y., Kanatzidis, M.G.: Analysis of nanostructuring in high figure-of-merit $Ag_{1-x}Pb_mSbTe_{2+m}$ thermoelectric materials. Adv. Funct. Mater. **19**, 1254–1259 (2009)
191. Ikeda, T., Collins, L.A., Ravi, V.A., Gascoin, F.S., Haile, S.M., Snyder, G.J.: Self-assembled nanometer lamellae of thermoelectric PbTe and Sb_2Te_3 with Epitaxy-like interfaces. Chem. Mater. **19**, 763 (2007)
192. Nguyen, P., et al.: Spark eroded $Bi_{0.5}Sb_{1.5}Te_3$ nanocomposites with enhanced thermoelectric performance and high production rate. Symposium JJ 2.6, MRS spring meeting and exhibition (2012), spark erosion: a high production rate method for producing Bi0.5Sb1.5Te3 nanoparticles with enhanced thermoelectric performance. Nanotechnology **23**, 415604 (2012)
193. Berkowitz, A.E., Walter, J.L.: Spark erosion: a method for producing rapidly quenched fine powders. J. Mater. Res. **2**, 277–288 (1987)
194. Carrey, J., Radousky, H.B., Berkowitz, A.E.: Spark-eroded particles: influence of processing parameters. J. Appl. Phys. **95**, 823 (2004)
195. Serrano-Sánchez, F., et al.: Enhanced figure of merit in nanostructured (bi, $Sb)_2Te_3$ with optimized composition. Sci. Rep. **7**, 6277 (2017)
196. Goldsmid, H.J.: The Improvement of a Specific Material-Bismuth Telluride, Introduction to Thermoelectricity, pp. 85–107. Springer, Berlin (2016)
197. Sootsman, J.R., Chung, D.Y., Kanatzidis, M.G.: New and old concepts in thermoelectric materials. Angew Chem. Int. Ed. **48**, 8616–8639 (2009)
198. Park, K.H., Mohamed, M., Aksamija, Z., Ravaioli, U.: Ab initio lattice dynamics and thermochemistry of layered bismuth telluride (Bi_2Te_3). J. Appl. Phys. **117**, 015103 (2015)
199. Tanaka, S., Takiishi, M., Miyazaki, K., Tsukamoto, H.: Measurements of thermal conductivity of thin films by 3-omega method. In: International Conference on Micro/Nanoscale Heat Transfer, pp. 477–483. ASME, New York (2008)
200. Xu, Z., et al.: Attaining high mid-temperature performance in (bi, $Sb)_2Te_3$ thermoelectric materials via synergistic optimization. NPG Asia Mater. **8**, e302 (2016)
201. Tritt, T.M.: Thermal Conductivity: Theory, Properties, and Applications, pp. 1–9. Springer, Berlin (2005)
202. Hasan, M.N., Wahid, H., Nayan, N., Ali, M.S.M.: Inorganic thermoelectric materials: a review. Int. J. Energy Res. **44**, 1–53 (2020)
203. Lan, Y., et al.: Structure study of bulk nanograined thermoelectric bismuth antimony telluride. Nano. Lett. **9**, 1419–1422 (2009)
204. Yan, X., et al.: Experimental studies on anisotropic thermoelectric properties and structures of n-Type $Bi_{(2)}Te_{(2.7)}Se_{(0.3)}$). Nano Lett. **10**, 3373–3378 (2010)
205. Cao, Y.Q., Zhao, X.B., Zhu, T.J., Zhang, X.B., Tu, J.P.: Syntheses and thermoelectric properties of $Bi_{(2)}Te_{(3)}/Sb_{(2)}Te_{(3)}$ bulk nano- composites with laminated nanostructure. Appl. Phys. Lett. **92**, 143106 (2008)
206. Xie, W., Tang, X., Yan, Y., Zhang, Q., Tritt, T.M.: Highthermo- electric performance BiSbTe alloy with unique low-dimensional structure. J. Appl. Phys. **105**, 113713 (2009)
207. Xie, W., Tang, X., Yan, Y., Zhang, Q., Tritt, T.M.: Unique nanostructures and enhanced thermoelectric performance of melt-spun BiSbTe alloys. Appl. Phys. Lett. **94**, 102111 (2009)
208. Sharma, S., Schwingenschlögl, U.: Thermoelectric response in single quintuple layer Bi_2Te_3. ACS Energy Lett. **1**, 875–879 (2016)
209. Zhai, R., Wu, Y., Zhu, T.-J., Zhao, X.-B.: Tunable optimum temperature range of high-performance zone melted bismuth-telluride-based solid solutions. Cryst Growth Des. **18**, 4646–4652 (2018)
210. Hao, F., et al.: Enhanced thermoelectric performance in n-type Bi_2Te_3-based alloys via suppressing intrinsic excitation. ACS Appl. Mater. Interfaces **10**, 21372–21380 (2018)

211. Yang, L., Chen, Z.-G., Hong, M., Han, G., Zou, J.: Enhanced thermoelectric performance of nanostructured Bi_2Te_3 through significant phonon scattering. ACS Appl. Mater. Interfaces **7**, 23694–23699 (2015)
212. Xu, B., Feng, T., Li, Z., Zhou, L., Pantelides, S.T., Wu, Y.: Creating zipper-like van der Waals gap discontinuity in low-temperature- processed nanostructured $PbBi_{2n}Te_{1+3n}$: enhanced phonon scattering and improved thermoelectric performance. Angew Chem. Int. Ed. **57**, 10938–10943 (2018)
213. Soni, A., Yanyuan, Z., Ligen, Y., Aik, M.K.K., Dresselhaus, M.S., Xiong, Q.: Enhanced thermoelectric properties of solution grown $Bi_2Te_{3-x}Se_x$ Nanoplatelet composites. Nano Lett. **12**, 1203–1209 (2012)
214. Hong, M., et al.: N -type $Bi_2Te_{3-x}Se_x$ Nanoplates with enhanced thermoelectric efficiency driven by wide-frequency phonon scatterings and synergistic carrier scatterings. ACS Nano **10**, 4719–4727 (2016)
215. Li, S., et al.: Graphene quantum dots embedded in Bi_2Te_3 Nanosheets to enhance thermoelectric performance. ACS Appl. Mater. Interfaces **9**, 3677–3685 (2017)
216. Yu, Y., et al.: Simultaneous optimization of electrical and thermal transport properties of $Bi_{0.5}Sb_{1.5}Te_3$ thermoelectric alloy by twin boundary engineering. Nano Energy **37**, 203–213 (2017)
217. Shalaby, M.S., et al.: Preparation, structural characteristics and optical parameters of the synthesized nano-crystalline sulphur-doped $Bi_2Te_{2.85}Se_{0.15}$ thermoelectric materials. J. Mater. Sci. Mater. Electron. **31**, 10612–10627 (2020)
218. Rashad, M.M., El-Dissouky, A., Soliman, H.M., Elseman, A.M., Refaat, H.M., Ebrahim, A.: Structure evaluation of bismuth telluride (Bi_2Te_3) nanoparticles with enhanced Seebeck coefficient and low thermal conductivity. Mater. Res. Innov. **22**, 315–323 (2018)
219. Kim, S.I., et al.: Dense dislocation arrays embedded in grain boundaries for high-performance bulk thermoelectrics. Science **348**, 109–114 (2015)
220. Shin, W.H., et al.: Enhanced thermoelectric performance of reduced graphene oxide incorporated bismuth-antimony-telluride by lattice thermal conductivity reduction. J. Alloys Compd. **718**, 342–348 (2017)
221. Cao, Y.Q., Zhao, X.B., Zhu, T.J., Zhang, X.B., Tu, J.P.: Syntheses and thermoelectric properties of Bi_2Te_3/Sb_2Te_3 bulk nanocomposites with laminated nanostructure. Appl. Phys. Lett. **92**, 143106 (2008)
222. Ji, X., Zhang, B., Tritt, T.M., Kolis, J.W., Kumbhar, A.: Solution-chemical syntheses of nanostructured Bi_2Te_3 and PbTe thermoelectric materials. J. Electron. Mater. **36**, 721–726 (2007)
223. Ji, X.H., He, J., Su, Z., Gothard, N., Tritt, T.M.: Improved thermoelectric performance in polycrystalline p-type Bi_2Te_3 via an alkali metal salt hydrothermal nanocoating treatment approach. J. Appl. Phys. **104**, 034907 (2008)
224. Fan, S., Zhao, J., Guo, J., Yan, Q., Ma, J., Hng, H.H.: p-type $Bi_{(0.4)}Sb_{(1.6)}Te_{(3)}$ nanocomposites with enhanced figure of merit. Appl. Phys. Lett. **96**, 182104 (2010)
225. Fan, X.A., et al.: Bi_2Te_3 hexagonal nanoplates and thermoelectric properties of n- type Bi_2Te_3 nanocomposites. J. Phys. D Appl. Phys. **40**, 5975–5979 (2007)
226. Heremans, J.P., et al.: Enhancement of thermoelectric efficiency in PbTe by distortion of the electronic density of states. Science **321**, 554–557 (2008)
227. Martin, J., Nolas, G.S., Zhang, W., Chen, L.: PbTe nanocomposites synthesized from PbTe nanocrystals. Appl. Phys. Lett. **90**, 222112 (2007)
228. Pei, Y., LaLonde, A., Iwanaga, S., Snyder, G.J.: High thermoelectric figure of merit in heavy hole dominated PbTe. Energy Environ. Sci. **4**, 2085–2089 (2011)
229. Zhang, Q., et al.: Heavy doping and band engineering by potassium to improve the thermoelectric figure of merit in p-type PbTe, PbSe, and $PbTe_{1-y}Se_y$. J. Am. Chem. Soc. **134**, 10031–10038 (2012)
230. Zhang, Q., et al.: Effect of aluminum on the thermoelectric properties of nanostructured PbTe. Nanotechnol. **24**, 345705 (2013)
231. Chere, E.K., et al.: Enhancement of thermoelectric performance in n-type PbTe1-ySey by doping Cr and tuning Te: Se ratio. Nano Energy **13**, 355–367 (2015)

232. Paul, B., Banerji, P.: The effect of chromium impurity on the thermoelectric properties of PbTe in the temperature range 100–600 K. J. Appl. Phys. **109**, 103710 (2011)
233. Sie, F.-R., Liu, H.-J., Kuo, C.-H., Hwang, C.-S., Chou, Y.-W., Yeh, C.-H.: Enhanced thermoelectric performance of n-type PbTe doped with Na_2Te. Intermetallics **92**, 113–118 (2018)
234. Jood, P., Ohta, M., Yamamoto, A., Kanatzidis, M.G.: Excessively doped PbTe with Ge-induced nanostructures enables high efficiency thermoelectric modules. Joule. **2**, 1339–1355 (2018)
235. Xiao, Y., et al.: Synergistically optimizing thermoelectric transport properties of n-type PbTe via se and Sn co-alloying. J. Alloys Compd. **724**, 208–221 (2017)
236. Shi, W., et al.: Tin selenide (SnSe): growth, properties, and applications. Adv. Sci. **5**, 1700602 (2018)
237. Chen, Z.-G., Shi, X., Zhao, L.-D., Zou, J.: High-performance SnSe thermoelectric materials: progress and future challenge. Prog. Mater. Sci. **97**, 283–346 (2018)
238. Zhou, Y., Zhao, L.D.: Promising thermoelectric bulk materials with 2D structures. Adv. Mater. **29**, 1702676 (2017)
239. Chen, Y.X., et al.: Understanding of the extremely low thermal conductivity in high-performance polycrystalline SnSe through potassium doping. Adv. Funct. Mater. **26**(37), 6836–6845 (2016)
240. Chandra, S., Biswas, K.: Realization of high thermoelectric figure of merit in solution synthesized 2D SnSe Nanoplates via Ge alloying. J. Am. Chem. Soc. **141**, 6141–6145 (2019)
241. Shi, X., et al.: High thermoelectric performance in p-type polycrystalline Cd-doped SnSe achieved by a combination of cation vacancies and localized lattice engineering. Adv. Energy Mater. **9**, 1803242 (2019)
242. Liu, J., et al.: Achieving high thermoelectric performance with Pb and Zn codoped polycrystalline SnSe via phase separation and nanostructuring strategies. Nano Energy **53**, 683–689 (2018)
243. Beretta, D., et al.: Thermoelectrics: from history, a window to the future. Mater. Sci. Eng. R Rep. **138**, 100501 (2018)
244. Chang, C., et al.: 3D charge and 2D phonon transports leading to high out-of-plane ZT in n-type SnSe crystals. Science **360**, 778–783 (2018)
245. Das, A., Kumar, A., Banerji, P.: First principles study of electronic structure and thermoelectric transport in tin selenide and phase separated tin selenide-copper selenide alloy. J. Phys. Condens. Matter. **32**, 265501 (2020)
246. Liu, H., et al.: Ultrahigh thermoelectric performance by electron and phonon critical scattering in $Cu_2Se_{1-x}I_x$. Adv. Mater. **25**, 6607–6612 (2013)
247. Byeon, D., et al.: Discovery of colossal seebeck effect in metallic Cu_2Se. Nat. Commun. **10**, 1–7 (2019)
248. Li, D., et al.: Chemical synthesis of nanostructured Cu2Se with high thermoelectric performance. RSC Adv. **4**, 8638–8644 (2014)
249. Hu, Q., Zhu, Z., Zhang, Y., Li, X.J., Song, H., Zhang, Y.: Remarkably high thermoelectric performance of Cu_{2-x} Li_xSe bulks with nanopores. J. Mater. Chem. A. **6**, 23417–23424 (2018)
250. Yang, L., Chen, Z.-G., Han, G., Hong, M., Zou, Y., Zou, J.: High performance thermoelectric Cu_2Se nanoplates through nanostructure engineering. Nano Energy **16**, 367–374 (2015)
251. Hu, Q., Zhang, Y., Zhang, Y., Li, X.J., Song, H.: High thermoelectric performance in Cu_2Se/CDs hybrid materials. J. Alloys Compd. **813**, 152204 (2020)
252. Li, M., et al.: Ultra-high thermoelectric performance in graphene incorporated Cu_2Se: role of mismatching phonon modes. Nano Energy **53**, 993–1002 (2018)
253. Li, M., et al.: Ultrahigh figure-of merit of Cu2Se incorporated with carbon coated boron nanoparticles. Info. Mat. **1**, 108–115 (2019)
254. Nolas, G.S., Cohn, J.L., Slack, G.A.: Effect of partial void filling on the lattice thermal conductivity of skutterudites. Phys. Rev. B **58**, 164–170 (1998)
255. Uher, C.: Skutterudites: prospective novel thermoelectrics. In: Tritt, T.M. (ed.) Semiconductors and Semimetals, vol. 69, pp. 139–253. Academic Press, San Diego, CA (2001)

256. Beretta, D., et al.: Thermoelectrics: From history, a window to the future. Mater Sci Eng R Rep. **138**, 100501 (2019)
257. Zhang, Q., et al.: Realizing high-performance thermoelectric power generation through grain boundary engineering of skutterudite-based nanocomposites. Nano Energy **41**, 501–510 (2017)
258. Zong, P.-A., et al.: Skutterudite with graphene-modified grain-boundary complexion enhances zT enabling high-efficiency thermoelectric device. Energy Environ. Sci. **10**, 183–191 (2017)
259. Khovaylo, V., Korolkov, T., Voronin, A., Gorshenkov, M., Burkov, A.: Rapid preparation of Inx Co_4Sb_{12} with a recordbreaking ZT=1.5: the role of the in overfilling fraction limit and Sb over stoichiometry. J. Mater. Chem. A. **5**, 3541–3546 (2017)
260. Lei, Y., et al.: Structure and thermoelectric performance of Ti-filled and Te-doped skutterudite $Ti_xCo_4Sb_{11.5}Te_{0.5}$ bulks fabricated by combination of microwave synthesis and spark plasma sintering. Mater. Lett. **233**, 166–169 (2018)
261. Hu, C., et al.: Effects of partial La filling and Sb vacancy defects on $CoSb_3$ skutterudites. Phys. Rev. B. **95**, 165204 (2017)
262. Sales, B.C.: Filled skutterudites. In: Gschneidner, K.A., Jr., Bünzli, J.-C.G., Pecharsky, V.K. (eds.) Handbook on the Physics and Chemistry of Rare Earths, vol. 33, pp. 1–34. Elsevier, Amsterdam (2003)
263. Rull-Bravo, M., Moure, A., Fernandez, J., Martin-Gonzalez, M.: Skutterudites as thermoelectric materials: revisited. RSC Adv. **5**, 41653–41667 (2015)
264. He, Q., et al.: Nanostructured thermoelectric skutterudite $Co_{1-x}Ni_xSb_3$ alloys. J. Nanosci. Nanotechnol. **8**, 4003–4006 (2008)
265. Chen, B., et al.: Low-temperature transport properties of the filled skutterudites CeFe4−xCoxSb12. Phys. Rev. B **55**, 1476–1480 (1997)
266. Keppens, V., et al.: Localized vibrational modes in metallic solids. Nature **395**, 876–878 (1998)
267. Puyet, M., Lenoir, B., Dauscher, A., Dehmas, M., Stiewe, C., Müller, E.: High temperature transport properties of partially filled $Ca_xCo_4Sb_{12}$ skutterudites. J. Appl. Phys. **95**, 4852–4855 (2004)
268. Chen, L.D., et al.: Anomalous barium filling fraction and n-type thermoelectric performance of Bay Co_4Sb_{12}. J. Appl. Phys. **90**, 1864–1868 (2001)
269. Li, H., Tang, X., Zhang, Q., Uher, C.: Rapid preparation method of bulk nanostructured $Yb_{0.3}Co_4Sb_{12+y}$ compounds and their improved thermoelectric performance. Appl. Phys. Lett. **93**, 252109 (2008)
270. Nolas, G.S., Kaeser, M., Littleton, R.T., Tritt, T.M.: High figure of merit in partially filled ytterbium skutterudite materials. Appl. Phys. Lett. **77**, 1855–1857 (2000)
271. Geng, H.Y., Ochi, S., Guo, J.Q.: Solidification contraction-free synthesis for the $Yb_{0.15}Co_4Sb_{12}$ bulk material. Appl. Phys. Lett. **91**, 022106 (2007)
272. Ur, S.-C., Kwon, J.-C., Kim, I.-H.: Thermoelectric properties of tin-filled skutterudites prepared by mechanical alloying process. Met. Mater. Int. **14**, 625–629 (2008)
273. Bao, S., et al.: Preparation of La-filled skutterudites by mechanical alloying and hot pressing and their thermal conductivities. Mater. Sci. Eng. A **438–440**, 186–189 (2006)
274. Bao, S., Yang, J., Zhu, W., Fan, X., Duan, X., Peng, J.: Preparation and thermoelectric properties of La filled skutterudites by mechanical alloying and hot pressing. Mater. Lett. **60**, 2029–2032 (2006)
275. Zhou, C., Sakamoto, J., Morelli, D., Zhou, X., Wang, G., Uher, C.: Thermoelectric properties of $Co_{0.9}Fe_{0.1}Sb_3$-based skutterudite nanocomposites with $FeSb_2$ nano-inclusions. J. Appl. Phys. **109**, 063722 (2011)
276. Nolas, G.S., Wang, D., Beekman, M.: Transport properties of polycrystalline $Mg_2Si_{1-y}Sb_y$ ($0 \leq y < 0.4$). Phys. Rev. B **76**, 235204 (2007)
277. Huang, Y., et al.: Synthesis, structural and photoluminescence properties of Mg2Si/Si nanocomposites consisting of Si nanosheet bundles and Mg2Si deposits. Jpn. J. Appl. Phys. **58**, SBBK04 (2019)

278. Zaitsev, V.K., et al.: Highly effective $Mg_2Si_{1-x}Sn_x$ thermoelectrics. Phys. Rev. B **74**, 045207 (2006)
279. Zhang, Q., He, J., Zhu, T.J., Zhang, S.N., Zhao, X.B., Tritt, T.M.: High figures of merit and natural nanostructures in $Mg_2Si_{0.4}Sn_{0.6}$ based thermoelectric materials. Appl. Phys. Lett. **93**, 102109 (2008)
280. Souda, D., Shimizu, K., Ohishi, Y., Muta, H., Yagi, T., Kurosaki, K.: High thermoelectric power factor of Si–Mg_2Si nanocomposite ribbons synthesized by melt spinning. ACS Appl. Energy Mater. **3**, 1962–1968 (2020)
281. Ioffe, A.F.: Physics of Semiconductors. Academic Press, New York (1960)
282. Slack, G.A., Hussain, M.A.: The maximum possible conversion efficiency of silicon–germanium thermoelectric generators. J. Appl. Phys. **70**, 2694–2718 (1991)
283. Mu, X., Wang, L., Yang, X., Zhang, P., To, A.C., Luo, T.: Corrigendum: ultra-low thermal conductivity in Si/Ge hierarchical Superlattice nanowire. Sci. Rep. **6**, 32904 (2016)
284. Wang, W., Zhang, G.Q., Li, X.G.: Manipulating growth of thermoelectric Bi2Te3/Sb multilayered nanowire arrays. J. Phys. Chem. C **112**(39), 15190 (2008)
285. Usenko, A.A., et al.: Optimization of ball-milling process for preparation of Si-Ge nanostructured thermoelectric materials with a high figure of merit. Scr. Mater. **96**, 9–12 (2015)
286. Lan, Y., Ren, Z.: Thermoelectric nanocomposites for thermal energy conversion. In: Li, Q. (eds.) Nanomaterials for Sustainable Energy. NanoScience and Technology. Springer, Cham (2016). https://doi.org/10.1007/978-3-319-32023-6_11
287. Joshi, G., et al.: Enhanced thermoelectric figure of- merit in nanostructured p-type silicon germanium bulk alloys. Nano Lett. **8**, 4670–4674 (2008)
288. Donmez Noyan, I., et al.: SiGe nanowire arrays based thermoelectric microgenerator. Nano Energy **57**, 492–499 (2019)
289. Usenko, A., et al.: Enhanced thermoelectric figure of merit of p-type $Si_{0.8}Ge_{0.2}$ nanostructured spark plasma sintered alloys with embedded SiO_2 nanoinclusions. Scr. Mater. **127**, 63–67 (2017)
290. Peng, Y., et al.: Improved thermoelectric property of B-doped Si/Ge multilayered quantum dot films prepared by RF magnetron sputtering. Jpn. J. Appl. Phys. **57**, 01AF03 (2017)
291. Kikuchi, A., Yao, A., Mori, I., Ono, T., Samukawa, S.: Composite films of highly ordered Si nanowires embedded in $SiGe_{0.3}$ for thermoelectric applications. J. Appl. Phys. **122**, 165302 (2017)
292. Usenko, A., et al.: Thermoelectric properties and cost optimization of spark plasma sintered n-type $Si_{0.9}Ge_{0.1}$-Mg_2Si nanocomposites. Scr. Mater. **146**, 295–299 (2018)
293. Shuai, J., Mao, J., Song, S., Zhang, Q., Chen, G., Ren, Z.: Recent progress and future challenges on thermoelectric Zintl materials. Mater. Today Phys. **1**, 74–95 (2017)
294. Cooley, J.A., et al.: High Seebeck coefficient and unusually low thermal conductivity near ambient temperatures in layered compound $Yb_{2-x}Eu_xCdSb_2$. Chem. Mater. **30**, 484–493 (2017)
295. Hu, Y., Wang, J., Kawamura, A., Kovnir, K., Kauzlarich, S.M.: $Yb_{14}MgSb_{11}$ and $Ca_{14}MgSb_{11}$-new mg-containing Zintl compounds and their structures, bonding, and thermoelectric properties. Chem. Mater. **27**, 343–351 (2014)
296. Bhardwaj, A., Misra, D.: Enhancing thermoelectric properties of a p-type Mg_3Sb_2-based Zintl phase compound by Pb substitution in the anionic framework. RSC Adv. **4**, 34552–34560 (2014)
297. Kauzlarich, S.M., Brown, S.R., Snyder, G.J.: Zintl phases for thermoelectric devices. Dalton Trans. **2007**, 2099–2107 (2007)
298. Shi, X., Chen, L., Uher, C.: Recent advances in high-performance bulk thermoelectric materials. Int. Mater. Rev. **61**, 379–415 (2016)
299. Brown, S.R., et al.: Improved thermoelectric performance in $Yb_{14}Mn_{1-x}Zn_xSb_{11}$ by the reduction of spin-disorder scattering. Chem. Mater. **20**, 3412–3419 (2008)
300. Toberer, E.S., et al.: Traversing the metalinsulator transition in a Zintl phase: rational enhancement of thermoelectric efficiency in $Yb_{14}Mn_{1-x}Al_xSb_{11}$. Adv. Funct. Mater. **18**, 2795–2800 (2008)

301. Toberer, E.S., Brown, S.R., Ikeda, T., Kauzlarich, S.M., Jeffrey Snyder, G.: High thermoelectric efficiency in lanthanum doped $Yb_{14}MnSb_{11}$. Appl. Phys. Lett. **93**, 062110 (2008)
302. Snyder, G.J., Gascoin, F., Brown, S., Kauzlarich, S.: High efficiency thermoelectric power generation using Zintl-type materials. US Patent, 7728218 (2010)
303. Huang, D., et al.: Conjugated-backbone effect of organic small molecules for n-type thermoelectric materials with ZT over 0.2. J. Am. Chem. Soc. **139**, 13013–13023 (2017)
304. Shuai, J., et al.: Thermoelectric properties of bi based Zintl compounds $Ca_{1-x}Yb_xMg_2Bi_2$. J. Mater. Chem. A. **4**, 4312–4320 (2016)
305. Zhang, H., et al.: A new type of thermoelectric material, $EuZn_2Sb_2$. J Chem Phys. **129**, 164713 (2008)
306. Takagiwa, Y., et al.: Thermoelectric properties of $EuZn_2Sb_2$ Zintl compounds: zT enhancement through Yb substitution for Eu. J. Alloys Compd. **703**, 73–79 (2017)
307. Wei, P.-C., et al.: Enhancement of thermoelectric figure of merit in β-Zn_4Sb_3 by indium doping control. Appl. Phys. Lett. **107**, 123902 (2015)
308. Shuai, J., et al.: Thermoelectric properties of Na-doped Zintl compound: $Mg_{3-x}Na_xSb_2$. Acta Mater. **93**, 187–193 (2015)
309. Li, J., Zheng, S., Fang, T., Yue, L., Zhang, S., Lu, G.: Computational prediction of a high ZT of n-type Mg_3Sb_2-based compounds with isotropic thermoelectric conduction performance. Phys. Chem. Chem. Phys. **20**, 7686–7693 (2018)
310. Li, J., et al.: Designing high-performance n-type Mg_3Sb_2-based thermoelectric materials through forming solid solutions and biaxial strain. J. Mater. Chem. A. **6**, 20454–20462 (2018)
311. Bhardwaj, A., Chauhan, N.S., Misra, D.K.: Significantly enhanced thermoelectric figure of merit of p-type Mg_3Sb_2-based Zintl phase compounds via nanostructuring and employing high energy mechanical milling coupled with spark plasma sintering. J. Mater. Chem. A **3**, 10777 (2015)
312. Heusler, F.: Verh. Deutsche Physikalische Gesellschaft. **5**, S. 219 ff (1903)
313. Galanakis, I.: Theory of Heusler and Full-Heusler Compounds. In: Felser, C., Hirohata, A. (eds.) Heusler Alloys. Springer Series in Materials Science, vol. 222. Springer, Cham (2016). https://doi.org/10.1007/978-3-319-21449-8_1
314. Wollmann, L., Nayak, A.K., Parkin, S.S.P., Felser, C.: Heusler 4.0: tunable materials. Annu. Rev. Mater. Res. **47**, 247–270 (2017)
315. Gao, Q., Opahle, I., Zhang, H.: High-throughput screening for spin-gapless semiconductors in quaternary Heusler compounds. Phys. Rev. Mater. **3**, 024410 (2019)
316. Khandy, S.A., Chai, J.D.: Robust stability, half-metallic ferrimagnetism and thermoelectric properties of new quaternary Heusler material: a first principles approach. J. Magn. Magn Mater. **502**, 166562 (2020)
317. Khandy, S.A., Chai, J.D.: Thermoelectric properties, phonon, and mechanical stability of new half-metallic quaternary Heusler alloys: FeRhCrZ (Z = Si and Ge). J. Alloys Compd. **127**, 165102 (2020)
318. Maat, S., Marley, A.C.: Physics and design of hard disk drive magnetic recording read heads. In: Xu, Y., Awschalom, D., Nitta, J. (eds.) Handbook of Spintronics. Springer, Dordrecht (2016)
319. Chadov, S., Wu, S.C., Felser, C., Galanakis, I.: Stability of Weyl points in magnetic half-metallic Heusler compounds. Phys. Rev. B **96**, 024435 (2017)
320. Chang, G., et al.: Room-temperature magnetic topological Weyl fermion and nodal line semimetal states in half-metallic Heusler Co_2Ti_X (X= Si, Ge, or Sn). Sci. Rep. **6**, 38839 (2016)
321. Hinterleitner, B., et al.: Thermoelectric performance of a metastable thin-film Heusler alloy. Nature **576**, 85–90 (2019)
322. Joshi, G., et al.: NbFeSb-based p-type half-Heuslers for power generation applications. Energy Environ. Sci. **7**, 4070–4076 (2014)
323. Zhu, H., et al.: Discovery of TaFeSb-based half-Heuslers with high thermoelectric performance. Nat. Commun. **10**, 270 (2019)

324. Fu, C., et al.: High band degeneracy contributes to high thermoelectric performance in p-type half-Heusler compounds. Adv. Energy Mater. **4**, 1400600 (2014)
325. Kaur, K., Kumar, R.: Ti based half Heusler compounds: a new on the screen with robustic thermoelectric performance. J. Alloys Compd. **727**, 1171–1177 (2017)
326. Liu, Y., et al.: Demonstration of a phonon-glass electron-crystal strategy in (Hf, Zr) NiSn half-Heusler thermoelectric materials by alloying. J. Mater. Chem. **3**, 22716 (2015)
327. Chen, S., et al.: Effect of Hf concentration on thermoelectric properties of nanostructured N-Type half-Heusler materials HfxZr1–xNiSn0.99Sb0.01. Adv. Energy Mater. **3**, 1210 (2013)